2004

Dissolution of uranyl microprecipitates in subsurface sediments at Hanford Site, USA

Chongxuan Liu
Pacific Northwest National Laboratory, chongxuan.liu@pnl.gov

John M. Zachara
Pacific Northwest National Laboratory, john.zachara@pnl.gov

Odeta Qafoku
Pacific Northwest National Laboratory

James Mckinley
Pacific Northwest National Laboratory, james.mckinley@pnl.gov

Steve M. Heald
Pacific Northwest National Laboratory, steve.heald@pnl.gov

See next page for additional authors

Pergamon

Geochimica et Cosmochimica Acta, Vol. 68, No. 22, pp. 4519-4537, 2004

0016-7037/04 $30.00 + .00

doi:10.1016/j.gca.2004.04.017

Dissolution of uranyl microprecipitates in subsurface sediments at Hanford Site, USA

CHONGXUAN LIU,[1,*] JOHN M. ZACHARA,[1] ODETA QAFOKU,[1] JAMES P. MCKINLEY,[1] STEVE M. HEALD,[1,2] and ZHEMING WANG[1]

[1]Pacific Northwest National Laboratory, P.O. Box 999, MSIN K8-96, Richland, WA 99352, USA
[2]PNC-CAT Argonne National Laboratory, 9700 S. Cass Ave., Argonne, IL 60439, USA

(*Received December* 8, 2003; *accepted in revised form April* 26, 2004)

Abstract—The dissolution of uranium was investigated from contaminated sediments obtained at the US. Department of Energy (U.S. DOE) Hanford site. The uranium existed in the sediments as uranyl silicate microprecipitates in fractures, cleavages, and cavities within sediment grains. Uranium dissolution was studied in Na, Na-Ca, and NH_4 electrolytes with pH ranging from 7.0 to 9.5 under ambient CO_2 pressure. The rate and extent of uranium dissolution was influenced by uranyl mineral solubility, carbonate concentration, and mass transfer rate from intraparticle regions. Dissolved uranium concentration reached constant values within a month in electrolytes below pH 8.2, whereas concentrations continued to rise for over 200 d at pH 9.0 and above. The steady-state concentrations were consistent with the solubility of Na-boltwoodite and/or uranophane, which exhibit similar solubility under the experimental conditions. The uranium dissolution rate increased with increasing carbonate concentration, and was initially fast. It decreased with time as solubility equilibrium was attained, or dissolution kinetics or mass transfer rate from intraparticle regions became rate-limiting. Microscopic observations indicated that uranium precipitates were distributed in intragrain microfractures with variable sizes and connectivity to particle surfaces. Laser-induced fluorescence spectroscopic change of the uranyl microprecipitates was negligible during the long-term equilibration, indicating that uranyl speciation was not changed by dissolution. A kinetic model that incorporated mineral dissolution kinetics and grain-scale, fracture-matrix diffusion was developed to describe uranium release rate from the sediment. Model calculations indicated that 50–95% of the precipitated uranium was associated with fractures that were in close contact with the aqueous phase. The remainder of the uranium was deeply imbedded in particle interiors and exhibited effective diffusivities that were over three orders of magnitude lower than those in the fractures. *Copyright © 2004 Elsevier Ltd*

1. INTRODUCTION

Uranium (U) is a common subsurface contaminant at United States Department of Energy (DOE) sites resulting from its central role in the nuclear fuel cycle (Riley and Zachara, 1992). The geochemical behavior of U, including its reactive transport chemistry and potential for remediation, is a matter of concern and intensive research. Subsurface uranium mobility is controlled by adsorption to mineral materials and dissolution/precipitation of uranium solids. Uranium is hexavalent [U(VI)] under oxidized conditions and exists as the uranyl ion (UO_2^{2+}) and its complexes with various ligands in aqueous phase (Langmuir, 1978; Grenthe et al., 1992).

U(VI) is sorbed to fixed charge sites on phyllosilicates by ion exchange (McKinley et al., 1995; Turner et al., 1996), and to hydroxylated mineral surfaces including the edges of phyllosilicates and Al(III), Fe(III), and Si(IV) oxides by complexation (Hsi and Langmuir, 1985; Waite et al., 1994; McKinley et al., 1995; Duff and Amrhein, 1996; Hudson et al., 1999; Payne et al., 1996; Turner et al., 1996; Bargar et al., 1999, 2000; Lenhart and Honeyman, 1999; Sylwester et al., 2000; Davis et al., 2002). The U(VI) adsorption process is often described using equilibrium surface complexation models (e.g., McKinley et al., 1995; Waite et al., 2000; Davis et al., 2002).

Studies of U(VI) desorption are limited. The desorption rate of U from laboratory-spiked pristine materials (Fuhrmann et al., 1997; Ohnuki et al., 1997; Giammar and Hering, 2001) and U-contaminated sediments (Braithwaite et al., 1997; Mason et al., 1997) was found to decrease with increasing exposure time to uranium contamination. For example, desorption equilibrium of U(VI) from goethite after aging for 1 month was achieved rapidly, but much slower desorption was observed after aging for 6 months (Giammar and Hering, 2001). Braithwaite et al. (1997) observed that the desorption half-life for sediments that were exposed to the long term U(VI) contamination was more than 10 yr. Slow desorption kinetics are generally attributed to diffusion from and/or occlusion of U(VI) within intraparticle regions, or reduction to U(IV). Little is known about the influences of speciation, sorptive location and mineral phases, and diffusion on U(VI) release from contaminated sediments.

Investigations of the rates of uranyl mineral dissolution and of the factors influencing the rates are also limited. One laboratory study indicated that U(VI) mineral dissolution was influenced by the nature of complexing ligands and their strength of binding U(VI) (Sowder et al., 2001). The dissolution rates of metashoepite $[(UO_2)_8O_2(OH)_{12}\ (H_2O)_{10}]$ and becquerelite $[Ca(UO_2)_6O_4(OH)_6(H_2O)_8]$ were faster than those for metaautunites $[Ca(UO_2)_2(PO_4)_2(H_2O)_x]$ and chernikovite $[UO_2HPO_4(H_2O)_4]$ in solutions of acetic acid and EDTA, while becquerelite and chernikovite were slower than metashoepite and metaautunite in bicarbonate solutions. Higher concentrations of complexants, including bicarbonate, caused more rapid dissolution. The rate and extent of dissolution of U(VI)-oxides (Steward and Mones,

* Author to whom correspondence should be addressed, at (Chongxuan.liu@pnl.gov).

1997), uranophane [$Ca(UO_2)_2(SiO_3OH)_2(H_2O)_5$] (Perez et al., 2000), and soddyite [$(UO_2)_2SiO_4(H_2O)_2$] (Perez et al., 1997) all increase with increasing bicarbonate concentration.

In this communication, the rate and extent of uranyl dissolution was measured from three Hanford vadose zone sediments that had been contaminated by a high level nuclear waste discharge over 50 years ago. The uranium in the sediments existed as discontinuous particle coatings and intragrain precipitates of uranyl silicates primarily in plagioclase-containing clast fragments (McKinley et al., 2002; Wang et al., 2004). Our objectives were to quantify physical, mineralogic, chemical, and thermodynamic factors controlling U release to the aqueous phase. Dissolution was studied over a range of pH and electrolyte concentration representative of the calcareous geochemical environment from which the samples were obtained. A kinetic model involving carbonate-mediated dissolution kinetics and diffusion from intragrain fracture domains was developed to provide insights on factors controlling the slow observed release rates and incomplete extent of U dissolution from the three sediments.

2. MATERIALS AND METHODS

2.1. Contaminated Sediments

Uranium-contaminated sediments were obtained from a borehole (299-E33-45) at the Hanford BX tank farm that was drilled through a vadose zone waste plume proximate to tank BX-102 in 2001 to provide information on the depth distribution and inventory of uranium and technetium (Serne et al., 2002). The sediments selected for study are multilithologic and sand-textured, and originated in the Pleistocene catastrophic flood deposits of the Hanford formation. The sediments consist of 48% quartz, feldspar, and mica, 2% fines including expansible phyllosilicates. Over 50% of the sediment is basaltic lithic fragments (Serne et al., 2002).

An estimated 350 m^3 of waste solution containing over 7000 kg of U(VI) was discharged to the vadose zone in 1951 in the BX tank farm as a result of the overfilling of tank BX-102. This aqueous solution contained nominal concentrations of 2.5 to 5 mol/L Na_2CO_3, 0.36 mol/L PO_4, and virtually all fission products of uranium except plutonium with pH of approximately 10 (Jones et al., 2001). Characterization of the vadose zone near tank BX-102 has defined an extensive plume containing cesium, uranium, and other contaminants. The uranium was most abundant at depths between 21 and 52 m below ground surface (bgs) in borehole 299-E33-45 (Fig. 1). The maximum concentration of ^{238}U was 1649 μg/g. The studied samples were from three depths in the borehole: I53 (36 m bgs), I61 (40 m bgs), and I67 (43 m bgs) with total uranium concentrations ranging from 112 to 404 μg/g (Table 1). There were no significant differences in moisture content and major element concentrations between the samples (Table 1). The water saturation of the samples was calculated to be 16 to 21% of the sediment porosity assuming solid density of 2.67 g/cm^3 and sediment porosity of 0.32.

2.2. Pore-Water Analyses and Modeling

Chemical analyses of pore waters (Table 2) from unsaturated vadose zone sediments (I55, I61, and I64, Fig. 1) proximate to the three contaminated sediments (I53, I61, and I67) were obtained from Serne et al. (2002). These pore waters were obtained by ultracentrifugation in an unsaturated flow apparatus (UFA). The ultracentrifugation process is a relatively complicated one that is not free of artifacts. Briefly, core sediments were removed from the split spoon sampler, and were homogenized and packed into a UFA Teflon cell of approximate 35 cm^3 volume. The cell was spun over 5000 rcf for 8 h to yield a small volume of pore water. The pH and ion composition of the pore water were measured by accepted techniques (Serne et al., 2002). Precautions were not taken to prevent CO_2 degassing.

The reported chemical analyses were subject to aqueous speciation and saturation state analyses using the MINTEQA2 code (Allison et al., 1998) and a thermodynamic data base assembled by us from the literature. The reported analyses yielded an acceptable anion-cation balance, but the computed speciation was in gross supersaturation with

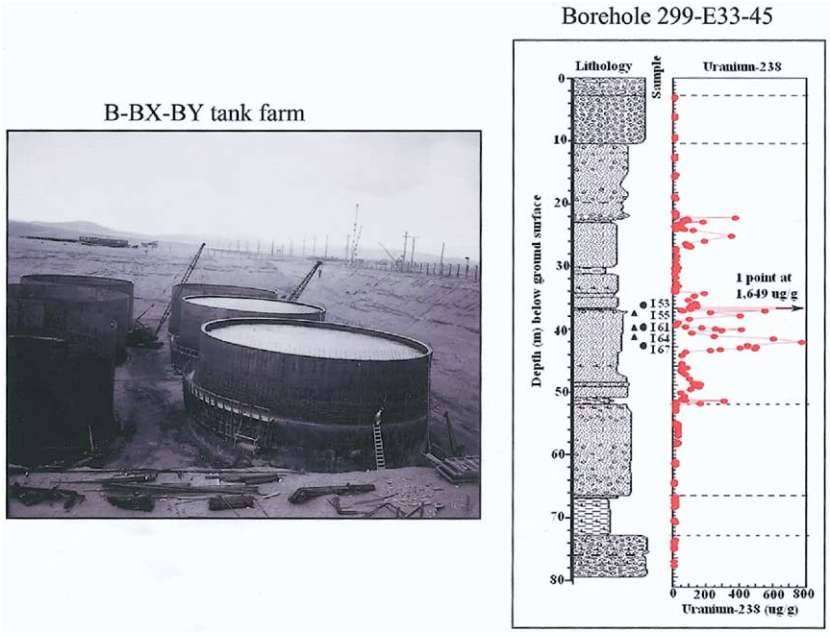

Fig. 1. The photograph (left plot) shows the BX tank farm under construction. Tank BX-102 is the middle on the right. The right plot shows the distribution of uranium in Borehole 299-E33-45 (near Tank BX-102). The collection depths for the sediment (circle) and pore water (triangle) samples are noted at 35-45m. The borehole was located approximately 9 m to the right of BX-102.

Table 1. Sediment characterization.[a]

	g/100 g					μmol/g			g/100g
Sediment	Al	Si	K	Ca	Fe	U	Sr	Mn	Moisture content
I53	6.51	32.7	2.11	2.9	3.54	0.47	4.37	12.16	2.80
I61	6.59	32.9	2.07	2.9	3.64	1.70	4.53	12.45	3.63
I67	6.52	32.7	2.04	2.86	3.23	1.37	4.55	9.83	2.75

[a] U concentration was measured by X-ray florescence (XRF). Other data from Serne et al., (2002).

respect to calcite. Hanford vadose zone pore waters and groundwaters are invariably in equilibrium with calcite that exists as a minor mineralogic component of all subsurface sediments. MINTEQA2 calculations were then performed to identify the pH by trial-and-error that yielded calcite equilibrium. The identification process started with a trial pH for a specific pore-water sample (e.g., I55, I61, or I64 in Table 2). The trial pH and the analytical data for anions and cations including total inorganic carbonate (Table 2) were used by MINTEQA2 to calculate the pore-water speciation, which was used to calculate calcite saturation index [log (IAP/K_{sp}), where IAP is the ionic activity product and K_{sp} is the solubility product of calcite]. If the calculated calcite saturation index was larger than zero a lower pH was tried at next step and vice versa. This procedure was iterated until a pH was identified that led to the absolute value of the calculated saturation index of calcite less than 0.001. The pore-water speciation correspondent to the identified pH was used to compute the pCO_2 in the pore water and the saturation state of various uranyl minerals (Table 2).

The aqueous complexation constants for U(VI) in our database were from (Guillaumount et al., 2003). The species $Ca_2UO_2(CO_3)_3^0$ was also included in the calculation with its constant from Kalmykov and Choppin (2000). Free energies of formation for known uranyl silicates ($\Delta_f G^o_m$) were tabulated (Table 3) from the literature or were estimated using the regression method of Chen et al. (1999). The free energies and solubilities of the uranyl silicates have not been well studied. The literature and calculated values were used along with those for other component species from Guillaumount et al. (2003) to calculate equilibrium solubility constants for the uranyl silicates (Table 3).

Table 2. Measured porewater composition and computed pH, pCO_2, and mineral saturation states.[a]

Component	I55	I61	I64
UO_2^{2+}	2.81×10^{-3}	1.85×10^{-3}	1.04×10^{-2}
K^+	1.23×10^{-3}	3.89×10^{-4}	1.46×10^{-3}
Na^+	1.35×10^{-1}	5.31×10^{-2}	1.98×10^{-1}
Ca^{2+}	9.53×10^{-4}	7.11×10^{-4}	4.02×10^{-3}
Mg^{2+}	1.16×10^{-3}	1.90×10^{-4}	5.80×10^{-4}
Cl^-	1.58×10^{-3}	4.51×10^{-4}	3.41×10^{-3}
NO_3^-	3.35×10^{-2}	5.69×10^{-3}	6.34×10^{-2}
SO_4^{2-}	1.56×10^{-2}	2.62×10^{-3}	3.39×10^{-2}
PO_4^{3-}	3.45×10^{-3}	1.63×10^{-3}	2.32×10^{-4}
H_4SiO_4	3.74×10^{-4}	7.16×10^{-4}	3.21×10^{-4}
HCO_3^-	7.21×10^{-2}	4.11×10^{-2}	6.53×10^{-2}
pH_m	9.35	9.06	9.16
pH_c	7.08	7.30	6.96
pCO_{2c}	−0.63	−1.07	−0.81
$(A\text{-}C)_a$ (%)	19.5	24.3	6.68
$(A\text{-}C)_s$ (%)	0.33	0.59	0.95
SI: Uranophane	−4.49	−2.37	−1.97
SI: Na-boltwoodite	−1.33	−0.60	−0.12
SI: Soddyite	−5.62	−4.19	−3.23
SI: Weeksite	−24.31	−22.33	−22.21
SI: Na-Weeksite	−5.85	−3.65	−3.57
SI: $SiO_{2(am)}$	−0.75	−0.51	−0.80

[a] Solute data (mol/L) from (Serne et al., 2002); pH_m, pH_c, and pCO_{2c} are the measured pH, computed pH, and computed CO_2 partial pressure (atm), respectively (see text); $(A\text{-}C)_a$ (%) and $(A\text{-}C)_s$ (%) are the percentage differences between total anion and cation equivalents for the analytical solutes with the measured pH and after speciation calculation using the calculated pH ($_pH_c$), respectively. SI is the mineral saturation index [log (IAP/K_{sp})].

2.3. Electrolyte Preparation

Sodium nitrate/bicarbonate solutions ranging between pH = 7 to 9.5 with ionic strength (I) = 0.05 and in equilibrium with atmospheric CO_2(g) were synthesized by appropriate additions of $NaNO_3$, $NaHCO_3$, NaOH, or HNO_3 (Table 4). The electrolytes were purged with air for at least 1 week to attain carbon dioxide equilibrium with slight pH adjustments to attain the desired pH values (e.g., pH increments of 0.5 pH unit). Electrolyte pH was stable after this time period. A similar set of electrolyte solutions ranging from pH 7.0 to 9.0 was made to be in equilibrium with calcite ($CaCO_3$) from $Ca(ClO_4)_2$, $NaHCO_3$, Na_2CO_3, NaOH, or $HClO_4$, and $CaCO_{3(s)}$ (Table 4). These solutions were open to the atmosphere and were allowed to equilibrate with $CaCO_{3(s)}$ for over 12 months. The calcite-equilibrated solutions had stable pH and were filtered through 0.22 μm-GV Millipore filters to remove solid-phase calcite before use in dissolution experiments.

2.4. Dissolution Kinetics

The time-dependent dissolution of U(VI) was studied at initial pH values of 7.5 and 9.5 in the Na-NO_3-HCO_3 and Na-Ca-ClO_4-HCO_3 electrolyte solutions at a sediment/solution ratio of 200 g/L. Replicate samples of field-moist sediments were mixed with the electrolyte solutions in acid-washed Teflon centrifuge tubes. The sediments were not air-dried before experimentation to avoid any changes to U(VI) speciation. The sediment suspensions were agitated in a rotating shaker (50 rpm) at room temperature.

After reaction times ranging from hours to 200 d, the suspensions were removed from the shaker, and were centrifuged at 5000 rcf for 20 min. A 0.2 mL aliquot of supernatant was removed and acidified with 0.1 mol/L HNO_3. Extensive pretesting with a variety of filters (0.1–0.2 μm) and centrifugation speeds documented that the phase separation scheme used above provided aqueous samples free of uranium-containing colloids. The experiment was designed so that repeated sample removal would have little or no change on the solid-to-solution ratio. In practice, this ratio changed by 6% over the course of the experiment. The acidified centrifuged samples were diluted and analyzed for U(VI) with a Kinetic Phosphorescence Analyzer (KPA) (Chemchek Instrument Inc., Richland, Washington). The detection limit of U(VI) with KPA was 4.9 ng/L. All standards and samples were prepared in 0.1 mol/L HNO_3 to provide a consistent sample matrix (Sowder et al., 1998). Aqueous samples with known U(VI) concentrations [500 and 1000 μg/L U(VI)] were used as control samples for each pH and electrolyte to evaluate the potential adsorption of uranium to the walls of the acid-washed Teflon centrifuge tubes for sediment equilibrations. No such adsorption was observed in any electrolyte during the course of the experiment.

At the end of the dissolution experiment, the suspensions were centrifuged as described before and filtered through prewashed (30 mL electrolyte + 2 mL sample) Centriplus YM-30 centrifugal filters (Millipore, MA), which do not sorb aqueous uranyl. The aqueous phase was analyzed for U(VI) before and after filtration. There was no indication for the presence of suspended uranium-containing colloids. The super-

Table 3. Free energy of formation and solubility product constants of some uranyl silicates.

Solid phase	$\Delta_f G^o_m$ (kJ/mol)	Dissolution Reaction	log K_{sp}[a]
Na-Boltwoodite	−2844.8(M)[1]	$Na[UO_2(SiO_3OH)](H_2O)_{1.5} + 3H^+ = UO_2^{2+} + Na^+ + H_4SiO_4 + 1.5H_2O$	5.82
Boltwoodite	−2814.4(C)[2]	$K[UO_2(SiO_3OH)](H_2O)_{1.5} + 3H^+ = UO_2^{2+} + K^+ + H_4SiO_4 + 1.5H_2O$	14.74
Uranophane	−6192.3(M)[3]	$Ca[UO_2(SiO_3OH)]_2(H_2O)_5 + 6H^+ = 2UO_2^{2+} + Ca^{2+} + 2H_4SiO_4 + 5H_2O$	11.70
Soddyite	−3653.0(M)[1]	$(UO_2)_2(SiO_4)(H_2O)_2 + 4H^+ = 2UO_2^{2+} + H_4SiO_4 + 2H_2O$	5.98
Na-Weeksite	−7993.9(M)[1]	$Na_2(UO_2)_2(Si_5O_{13})(H_2O)_3 + 6H^+ + 4H_2O = 2UO_2^{2+} + 2Na^+ + 5H_4SiO_4$	4.42
Weeksite	−7952.7(C)[2]	$K_2(UO_2)_2(Si_5O_{13})(H_2O)_3 + 6H^+ + 4H_2O = 2UO_2^{2+} + 2K^+ + 5H_4SiO_4$	18.84

[a] Solubility product constant (log K_{sp}) was calculated using $\Delta_f G^o_m$ of uranyl species and free energies of auxiliary components from Guillaumount et al. (2003). 1. Measured by Nguyen et al. (1992) and Moll et al. (1996) and recalculated by Chen et al. (1999). 2. Calculated using regression method of Chen et al. (1999). 3. Perez et al. (2000).

natant pH was immediately measured on a 1 mL aliquot of the supernatant sample. The supernatant was then acidified and analyzed for other elements (Na, Ca, Mg, Si, P) by ICP-AES. The total inorganic carbon was determined by coulometric titration (ASTM, 1988). The suspensions were also directly filtered through the prewashed filters and the filtrate and moist sediments (retained by the filter) were analyzed by time-resolved laser-induced fluorescence spectroscopy (TRLFS). Corresponding sediment duplicates were washed to remove soluble U(VI) with 2 mL of deionized water, centrifuged, and air dried for thin section preparations for X-ray microscopic examination.

2.5. Solubility Measurements

The contaminated sediments were equilibrated with the full suite of $Na\text{-}NO_3\text{-}HCO_3$ and $Na\text{-}Ca\text{-}ClO_4\text{-}HCO_3$ solutions (Table 4) at a sediment/solution ratio of 200 g/L to determine the solubility of uranium in the sediment samples. After reaction times of 65, 149, and 197 d, the suspensions were sampled, and U(VI) and pH were measured as described before. Na, Ca, Mg, Si, P, and inorganic C were determined on the aqueous samples collected at 197 d.

2.6. Dissolution in Ammonium Carbonate Solution

A strong uranyl complexant [0.5 mol/L $(NH_4)_2CO_3$) (Duff et al., 2002)] was used to expedite the rate and extent of uranium dissolution. After solubility measurements at pH 7.0 (section 2.5), the sediment was washed twice with and placed in 0.5 mol/L $(NH_4)_2CO_3$ at pH 8.4 with a suspension concentration of 200 g/L. Replicate suspensions were centrifuged for phase separation at selected times up to 450 h, and the supernatant U(VI) and pH were measured. The aqueous concentrations of Na, Ca, Mg, Si, P, and inorganic C were measured after 450 h of equilibration.

Table 4. Chemical compositions of electrolytes used in uranium dissolution experiments.[a]

	Na^+	NO_3^-	ClO_4^-	Ca^{2+}		
Electrolyte ID	(mmol/L)				Inorganic C	pH[b]
Na-1	50	49.9			0.08	6.95
Na-2	50	49.8			0.30	7.27
Na-3	50	49.4			0.71	7.61
Na-4	50	48.1			2.05	8.16
Na-5	50	43.5			6.82	8.67
Na-6	50	24.5			23.64	9.25
Ca-1[c]	2.1		122.9	61.81	0.34	7.02
Ca-2[c]	58.5		99.00	20.73	0.48	7.59
Ca-3[c]	81.9		82.55	1.84	1.42	8.05
Ca-4[c]	82.4		80.30	0.45	2.97	8.35
Ca-5[c]	43.8		41.04	0.38	2.40	8.37
Ca-6[c]	49.9		36.58	0.03	9.44	8.96

[a] All solutions were in equilibrium with atmospheric $CO_{2(g)}$.
[b] Final stable pH.
[c] Solutions were in equilibrium with $CaCO_{3(s)}$ as well as atmospheric $CO_{2(g)}$.

2.7. Spatial Distribution of Uranyl Phases

Thin sections of the contaminated sediments were prepared and analyzed by scanning electron microscopy (SEM), electron microprobe (EMP), and X-ray microprobe (XRM). A few g of sediment was imbedded in epoxy, wafered, affixed to a quartz slide, and polished for petrographic examination. Samples for SEM were carbon-coated for conductivity. The EMP and SEM analyses were combined as necessary to provide compositional and morphologic information concerning the occurrence and associations of uranium-bearing phases. Samples were examined using an accelerating potential of 20 keV, and compositional information was collected using either wavelength-dispersive (WDS) or energy dispersive spectrometers (EDS).

X-ray microprobe (XRM) measurements were performed at the Pacific Northwest Consortium-Collaborative Access Team (PNC-CAT) insertion device beamline (Heald et al., 1999) at the Advanced Photon Source (APS) at Argonne National Laboratory. Thin sections were mounted to an open stepper motor-driven stage on an optical bench and moved relative to the X-ray beam, which was focused by Kirkpatrick-Baez mirrors to a diameter of 6 μm on the sample surface. The X-ray flux was $\sim 5 \times 10^{11}$ photons/sec. False-color (blue to red) abundance maps were constructed for selected areas after normalizing detected X-rays to a measured current that was proportional to the primary flux. Fluorescent element-characteristic X-rays were detected with either WDS or EDS. Digital EMP, SEM, and XMP images were manipulated and merged using Photoshop (Adobe Systems).

3. RESULTS

3.1. Thermodynamic Calculations

Calculations using MINTEQA2 indicated that the reported pH of the displaced pore waters (Table 2) was inconsistent with the constraint of in-ground pore-water equilibrium with calcite and that $CO_2(g)$ degassed during the pore water extraction, manipulation, and analysis procedures. The computed pH's of the pore waters had to be reduced to approximately pH $\approx$ 7 to yield equilibrium with calcite. The computed pCO_2 values for these pore waters were quite high atm, ($\approx$0.1 Table 2). These high partial pressures of $CO_2(g)$ apparently resulted from waste-sediment reaction that involved the ion exchange displacement of adsorbed Ca^{2+} by high Na^+ in the waste solution and the resulting precipitation of calcite that lowered pH. The lower pH induced offgassing of $CO_2(g)$ from the waste solution that contained large concentrations of bicarbonate and carbonate.

The aqueous speciation of U(VI) in the pore waters and saturation states with respect to uranyl silicates were computed using our aqueous U(VI) speciation database and solubility

reactions in Table 3 along with the computed pH values. The aqueous species $UO_2(CO_3)_3^{4-}$ accounted for greater than 78% of the dissolved U in all of the pore waters, with the remainder occurring as $Ca_2UO_2(CO_3)_3^0$ and $UO_2(CO_3)_2^{2-}$. Aqueous species of U(VI) involving silicate, phosphate, hydroxide, chloride, and sulfate were minimal. The saturation index (log IAP/K_{sp}) with respect to Na-boltwoodite was closest to the equilibrium value of 0 among all of the uranyl silicates. However, Na-boltwoodite was consistently undersaturated in the pore water as was amorphous silica [SiO_2(am)].

3.2. Nature of Sediment Uranium

Uranium in Hanford sediment was found to be distributed as discrete precipitates within interiors of sediment grains (Fig. 2).

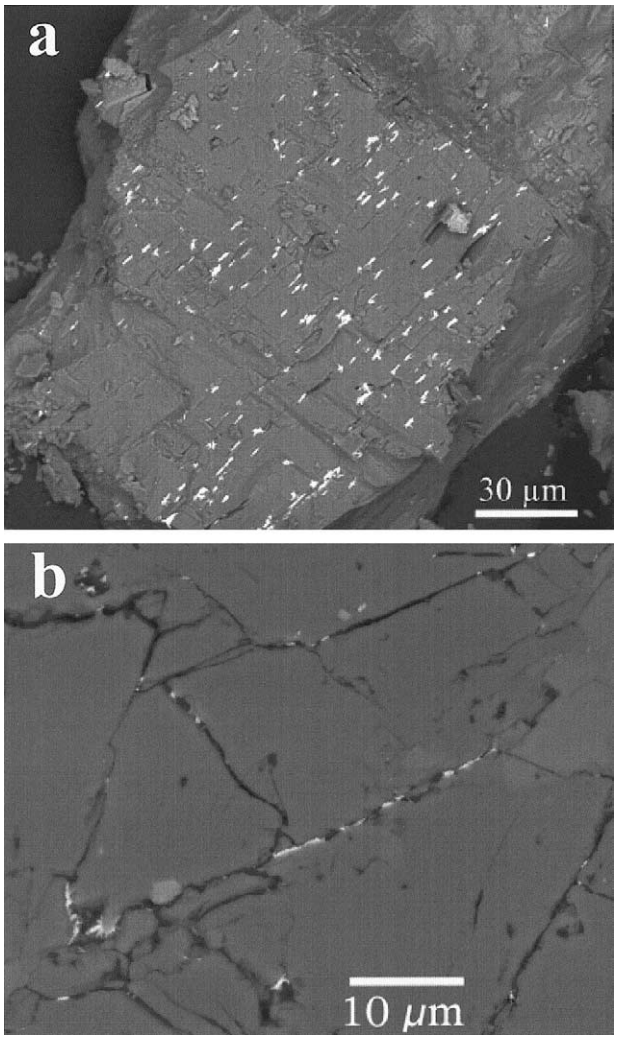

Fig. 2. Back-scattered-electron SEM images of sample I61 showing intraparticle uranium distribution within a plagioclase feldspar grain. Electron dense U(VI) precipitates appear white in the images. Image a) shows U(VI) crystallites that are aligned in parallel with cleavages on an intraparticle surface that was obtained by pressure-splitting the feldspar grain along a microfracture plane. Image b) shows U(VI) precipitates within microfractures in a thin section that was cut perpendicular to the fracture face in image a).

The precipitates were sparse on particle surfaces and were more abundant within microfractures of granitic lithic fragments, e.g., plagioclase feldspar (a minor component of the overall lithic fragment population) (McKinley et al., 2002). The precipitates were minute, generally less than 3 μm across, occurring as fine acicular crystals, in either radiating or parallel arrays in microfractures (Fig. 2). The precipitates were primarily aligned with two planes of microfractures meeting at or near 90 degree angles, consistent with two planes of plagioclase cleavage. The precipitates were distributed in microfractures of variable width and length.

X-ray adsorption near edge spectroscopy (XANES) indicated that only U(VI) was present in the sediment (Catalano et al., 2004; McKinley et al., 2002). Detailed analyses of both extended X-ray absorption fine structure (Catalano et al., 2004) and laser-induced fluorescence spectroscopy (Wang et al., 2004) indicated that the precipitates were uranyl silicates, most likely Na-boltwoodite or uranophane. The compositional analysis by energy dispersive X-ray spectroscopy (McKinley et al., 2002) also indicated that the precipitates were uranyl silicates, but likely Na-boltwoodite, Na-weeksite, or soddyite. The distinct fluorescence emission spectra of the sediment U was measured at liquid He temperature and its life-time did not change during dissolution (Wang et al., 2004). The presence of a single U-silicate phase was therefore implied within the sediment.

3.3. Uranium Solubility

The sediment uranyl-silicate phase dissolved to yield aqueous U(VI) concentrations of 8.4 to 231 μmol/L after 197 d of equilibration (Fig. 3). Dissolved U(VI) displayed two distinct regions: a constant concentration region below pH 8.2 and a region of increasing dissolved U(VI) above that pH. The uranyl concentrations varied significantly between the different samples, but the variation was insignificant between Na-NO_3-HCO_3 and Na-Ca-ClO_4-HCO_3 electrolytes. The uranyl concentration in the constant region (pH $<$ 8.2) was approximately 13–42 μmol/L and followed the sample order of I61 $>$ I67 $>$ I53. Above pH 8.5, dissolved U(VI) followed the sample order of I67 $>$ I61 $>$ I53. The concentrations of Na and/or Ca in the sediment suspensions at the end of equilibration (Appendix A, Tables A1 and A2) were only slightly different from those in the electrolytes (Table 4), indicating no significant dissolution or precipitation of sediment components during experimentation. Small changes were noted to suspension pH that resulted from the initial inequality in sediment and electrolyte pH values.

Uranyl speciation in the suspensions indicated that the increase of dissolved U above pH 8.2 was consistent with increasing $UO_2(CO_3)_3^{4-}$ concentration. The uranyl solubilities in the sediment suspensions were computed for Na-boltwoodite, uranophane, and several other plausible U phases (Fig. 3 and Appendix B, Tables B1 and B2). The calculations assumed that uranyl was congruently dissolved from only one phase (e.g., Na-boltwoodite, or uranophane, or other) and were made using the measured solution compositions at the end of equilibration (Appendix A, Tables A1 and A2). The total solid U(VI) concentrations available for dissolution were assumed to equal the total U content of the sediment (Table 1). Given the relatively

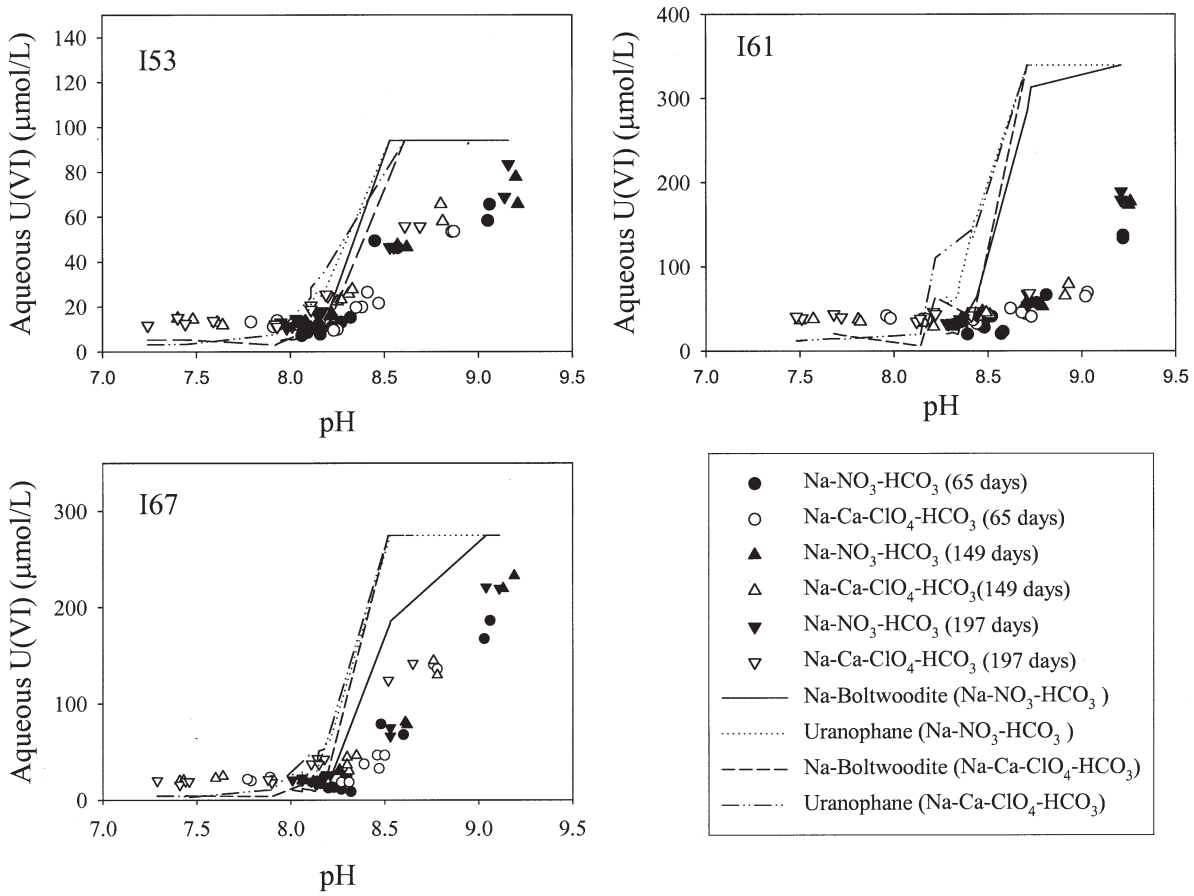

Fig. 3. Measured dissolved uranyl (symbols) and calculated uranyl solubility (lines) for samples I53, I61, and I67 in $Na\text{-}NO_3\text{-}HCO_3$ and $Na\text{-}Ca\text{-}ClO_4\text{-}HCO_3$ electrolytes with a sediment/water ratio of 200 g/L. Calculated solubilities are shown for Na-boltwoodite and uranophane.

low U_{TOT} in the sediments, the sediment U was computed to completely dissolve above pH 8.5 (e.g., horizontal line segments: Fig. 3, solid, dashed, dotted, and dot-dashed lines).

3.4. Uranyl Dissolution Kinetics

The rate of sediment U dissolution showed marked pH dependence and varied between sediments (Fig. 4). Uranyl concentrations increased slowly with time in the electrolytes with lower pH (<7.6) (Fig. 4) (the corresponding suspension pH values after ~200 d of dissolution are given in Appendix A, Tables A3 and A4). The measured uranyl concentrations at 200 d were consistent with those observed in the solubility experiments (Fig. 3). The U(VI) dissolution rate was higher near pH 9, and the overall release rate decreased with increasing equilibration time. The electrolyte composition did not appear to influence the dissolution rate. The leached uranium at Ph ≈ 9.0 represented 93, 57, and 90% of the total uranium in sediments I53, I61, and I67, respectively, after 200 d of contact with $Na\text{-}NO_3\text{-}HCO_3$ and $Na\text{-}Ca\text{-}ClO_4\text{-}HCO_3$ electrolytes.

The sediments displayed a rapid initial release of U(VI) in the suspensions near pH 9 (Fig. 4). The total U concentration released in this initial event for sediments I53 and I67 equaled that present in the pore water after adjusting for dilution by the added electrolyte solutions. The diluted U(VI) concentration was estimated to be 4.29, 13.43, and 8.99 μmol/L for samples I53, I61, and I67, respectively. The initial release of U(VI) from I61 was about double that attributable to pore water, suggesting the desorption of adsorbed U(VI) from the sediment at higher pH.

3.5. Uranium Dissolution in $(NH_4)_2CO_3$ Electrolyte

We suspected that uranyl release could be limited by the inaccessibility of microprecipitates in internal microfractures, and associated mass transfer limitation imposed on solute movement to and from these locations. Ammonium carbonate ($(NH_4)_2CO_3$, 0.5 mol/L) has been used as an extractant of U(VI) from sediments (Duff et al., 1998, 2000). It was used here to expedite U(VI) dissolution and its mass transfer rate from intraparticle regions. The rate of uranyl release (Fig. 5) by $(NH_4)_2CO_3$ increased by factors of 15 or more as compared to $Na\text{-}NO_3\text{-}HCO_3$ and $Na\text{-}Ca\text{-}ClO_4\text{-}HCO_3$ electrolytes (Fig. 4). Mass balance calculations indicated the release of 100, 69, and 93% of total uranium from sediments I53, I61, and I67, respectively. U release from sample I61 again showed a slow rate compared with the two other sediments. The suspension pH increased slowly from 8.4 to 9 (data not shown). The aqueous

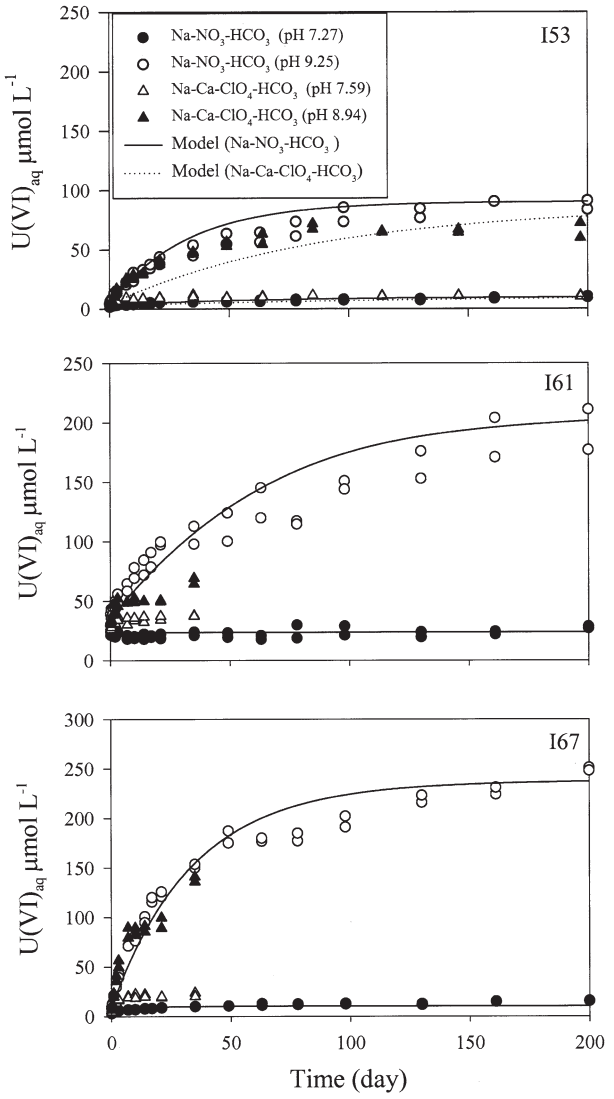

Fig. 4. Time-dependent dissolution of U(VI) from BX-102 sediments in Na-NO_3-HCO_3 and Na-Ca-ClO_4-HCO_3 electrolytes with a sediment/water ratio of 200g/L. Symbols and lines are experimental and modeling results, respectively. The electrolyte pH values are given in the figure legend. The corresponding suspension pH values after 200 d of dissolution are given in Tables A3 and A4 of Appendix A.

silicate, sodium, magnesium, and calcium concentrations were all higher after 19 d (Appendix A, Table A5), as a result of ion exchange and dissolution reactions.

4. DISCUSSION

4.1. Solubility of Uranyl Microprecipitates

Spectroscopic and microscopic studies collectively indicated that the sediment uranium phases were uranyl silicates, most likely uranophane group minerals or possibly soddyite or weeksite. X-ray absorption (Catalano et al., 2004) and laser fluorescence (Wang et al., 2004) analyses of the sediments indicated the presence of only one uranyl silicate phase in all of these sediments that remained unchanged with dissolution. Although Na-boltwoodite and uranophane most closely matched the spectroscopic results, the specific uranyl phase was not resolved because of the similar crystal structures of uranophane group minerals. Electron microprobe measurements of the composition of the uranyl silicate (McKinley et al., 2002) were not sufficiently precise to allow phase identification.

The measured uranyl concentrations in the batch solubility experiments were closest to the computed solubilities of Na-boltwoodite and uranophane (Fig. 3, Appendix A, Tables A1 and A2 and Appendix B, Tables B1 and B2), but significant differences existed. The computed pore water was close to saturation with to Na-boltwoodite (Table 2). The uranophane solubility was computed from a solubility constant (log K_{sp}) of 11.7 (Table 3), which was an average of the values measured for synthetic uranophane in bicarbonate solutions (10.75-12.94; Perez et al., 2000). A value of 9.42 ($\pm$0.48) was reported for synthetic uranophane in Na-ClO_4 electrolyte (Nguyen et al., 1992). The computation of Na-boltwoodite solubility used a log K_{sp} value of 5.82, which was reported as $\geq$ 5.82($\pm$0.16) in Na-ClO_4 electrolyte because of the formation of secondary soddyite during dissolution (Nguyen et al., 1992).

The disparity between the computed solubility of sediment U as either Na-boltwoodite or uranophane and the measured uranyl concentrations above pH 8.2 (Fig. 3) implied that the sediment U-silicate had not yet achieved dissolution equilibrium after 197 d of equilibration. This conclusion was supported by i.) the kinetic data in Figure 4 that showed continued dissolution of U (primarily from sediments I61 and I67) for 200 d without the attainment of steady-state concentration values and ii.) a lower than expected increase (e.g., slope) in measured uranyl concentration with increasing pH (Fig. 3). As a result of this apparent disequilibrium, the measured uranyl data did not allow for defensible evaluation as to whether the U-silicate free energies in Table 3 were or were not descriptive of the sediment U phase. The observation that $(NH_4)_2CO_3$ accelerated the release rate by factors of 15 or more (Figs. 4 and 5) implied that the kinetic dissolution rate of the U-silicate or mass transfer prevented the attainment of equilibrium above pH 8.2. The relative importance of these processes was tested

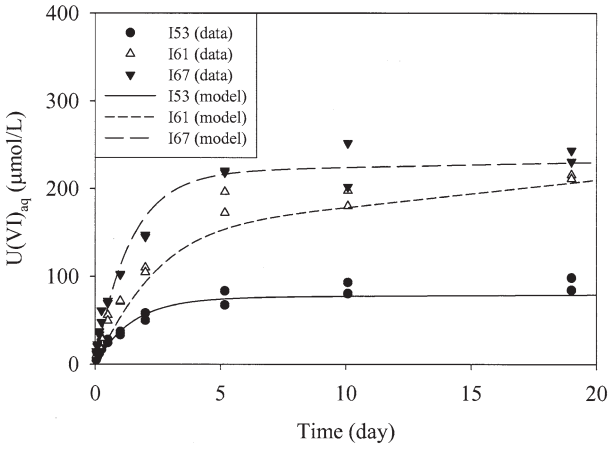

Fig. 5. Time-dependent dissolution of U(VI) from BX-102 sediments in 0.5 mol/L $(NH_4)_2CO_3$ electrolyte. The sediments were previously contacted with Na-Ca-ClO_4-HCO_3 electrolyte at pH 7.0 for 197 d before $(NH_4)_2CO_3$ extraction.

through kinetic and microscopic transport modeling described in Section 4.3.

The calculated uranyl solubility as either uranophane or Na-boltwoodite was generally lower than the measured values below pH 8.2 (Fig. 3). This result could not be attributed to dissolution kinetics, but could be explained by the variations in log K_{sp} given their large reported ranges. The reaction constants of Na-boltwoodite and uranophane were recalculated using following equations:
for uranophane:

$$K_{sp} = a^2_{UO_2^{2+}} a_{Ca^{2+}} a^2_{H_4SiO_4} a^{-6}_{H^+} \quad (1)$$

for Na-boltwoodite:

$$K_{sp} = a_{UO_2^{2+}} a_{Na^+} a_{H_4SiO_4} a^{-3}_{H^+} \quad (2)$$

where a_i is the activity of aqueous species i, that was calculated using the analytical data for each sample below pH 8.2 in Figure 3 and Tables A1 and A2. The calculated solubility product (log K_{sp}) for Na-boltwoodite and uranophane, respectively, were 6.15($\pm$0.06) and 11.58($\pm$0.18) in Na-NO_3-HCO_3 (sample number (n) = 13), and 6.04($\pm$0.61) and 12.55($\pm$0.80) in Na-Ca-ClO_4-HCO_3 (n = 28) electrolytes. The average values from all samples (n = 41) were 6.08($\pm$0.50) and 12.2($\pm$0.8) for Na-boltwoodite and uranophane, respectively. These log K_{sp} values were slightly higher than the literature values, but within the reported ranges.

4.2. Uranyl Release Processes

Uranyl dissolution from the contaminated sediments was a kinetic process characterized by an initial fast rate. This behavior could be explained by the coupled dissolution of the precipitates and solute mass transfer from intraparticle space. The pseudo–zero-order initial rates were 3.7, 5.5, 12.5 in Na-NO_3-HCO_3 electrolytes at high pH (Fig. 4) and 5.6, 94.1, and 182.4 (μmol/L)/d in $(NH_4)_2CO_3$ (Fig. 5) for samples I53, I61, and I67, respectively. The increase in uranyl mineral dissolution rate with increasing bicarbonate concentration has been observed for uranophane (Perez et al., 2000); soddyite (Perez et al., 1997); uranyl oxyhydroxides including metaschopite and becquerelite (Sowder et al., 2001) and $UO_3 \cdot H_2O$ and U_3O_8 (Steward and Mones, 1997); and uranyl phosphate including metaautunite and chernikovite (Sowder et al., 2001). Our results confirmed that the dissolution of the sediment U(VI) phase was promoted by aqueous bicarbonate.

A ligand (bicarbonate)-promoted mechanism has been used to describe uraninite dissolution in carbonate solution (Nicol and Needes, 1977; Hiskey, 1979, 1980; Sharma et al., 1996; Shoesmith et al., 1996a,b, 1989, 1998; Sunder et al., 1997; De Pablo et al., 1999). These studies showed that electron transfer, coordination of carbonate species on surface, and detachment of uranium-carbonate species from the surface were three steps controlling uraninite dissolution. According to these previous studies and our experimental data, we constructed a plausible model of uranyl dissolution from the Hanford sediments:

A. Coordinate carbonate species on U(VI) mineral surface

$$\equiv U(VI) + HCO_3^- \underset{k_{-1}}{\overset{k_1}{\Leftrightarrow}} \equiv U(VI) - HCO_3^- \quad (3)$$

B. Detachment of uranyl carbonate species from the mineral surface:

$$\equiv U(VI) - HCO_3^- \overset{k_2}{\Rightarrow} U(VI) - HCO_{3(aq)}^- \quad (4)$$

The detached aqueous U(VI) will rearrange its aqueous speciation in accordance with the solution composition and pH. Assuming that detachment (B) was rate-limiting, a kinetic rate expression from reactions 3 and 4 can be expressed as,

$$\frac{dU(VI)aq}{dt} = k_2 K_1 [\equiv U(VI)]\{HCO_3^-\} \quad (5)$$

where K_1 is the equilibrium constant for reaction 3; k_1 and k_{-1} are the forward and backward kinetic rate constants, respectively for reaction 3; k_2 is the forward rate constant for reaction 4; $\{HCO_3^-\}$ is the activity of HCO_3^-, and [$\equiv$ U(VI)] is the surface concentration of uranyl precipitates available for coordination with HCO_3^-.

Experimental studies of the dissolution kinetics of uranyl minerals in bicarbonate solutions have not uniformly agreed with the model described by Eqns. 3 to 5. The expression 5 predicts that dissolution rate is the first order with respect to bicarbonate activity when uranyl surface coordination sites remain constant. A rate expression proportional to carbonate concentration ($[HCO_3^-]^{0.7}$) was obtained for uranophane dissolution in batch and stirred flow systems (Perez et al., 2000). A rate order of 0.65 with respect to total carbonate concentration was observed from a regression analysis of the measured rates of uranyl oxyhydroxide dissolution in bicarbonate solutions (Steward and Mones, 1997). Our observation that the dissolution rate of U(VI) from Hanford sediment increased over 15 times when bicarbonate activity increased 17–20 times was approximately in line with the pseudo–first-order assumption. The regression studies of Perez et al. (2000) and Steward and Mones (1997) found that the influence of pH was not statistically significant compared with that of carbonate. The rate expression in Eqn. 5 implicitly assumed that the influence of pH was a result of variable bicarbonate concentration.

The reaction scheme of Eqns. 3 to 5 is appropriate when the solution composition is far from equilibrium. A comparable rate expression for near equilibrium includes an effective "free-energy" modifying term (e.g., Aagaard and Helgeson, 1982),

$$\frac{dU(VI)aq}{dt} = k'[\equiv U(VI)]\{HCO_3^-\}(1 - IAP/K_{sp}) \quad (6)$$

where $k' = k_2 K_1$; IAP is the ion activity product; and K_{sp} is the solubility constant. Both Eqns. 5 and 6 require a surface site concentration for the dissolving uranyl phase. Such information is difficult to obtain for a minor uranyl phase that is disseminated in sediment.

We assumed that the uranyl surface site concentration was proportional to the precipitated uranyl concentration, which yielded the following transformation of Eqn. 6:

$$\frac{dU(VI)_{aq}}{dt} = k[U(VI)_{solid}][HCO_3^-]_{tot}(1 - IAP/K_{sp}) \quad (7)$$

where $[U(VI)_{solid}]$ is the precipitated uranyl concentration (M) and k is an apparent rate parameter with a unit of (mol/L

of $[HCO_3^-]_{tot})^{-1}h^{-1}$. Because both CO_3^{2-} and HCO_3^- have a similar effect on solubilizing U(VI) from sediments (Mason et al., 1997), the rate expression 7 used total HCO_3^- ($[HCO_3^-]_{tot}$) (i.e., sum of CO_3^{2-} and HCO_3^- concentrations) as a proxy for $\{HCO_3^-\}$ in the following modeling.

Eqn. 7 implies that uranyl dissolution will decrease and cease when the dissolving phases approach equilibrium with the contacting electrolyte. Such behavior was noted in Figure 4 at pH = 7.3 and pH = 7.6 where U(VI) dissolution was both slow and limited. The initial U(VI) release was slightly larger than the calculated saturation concentration using log K_{sp} values in Table 3 for all samples and thus, there was only a slight increase in aqueous uranyl concentration during the entire dissolution experiment. These apparent steady state concentrations were better described using new solubility constants (log K_{sp}) for Hanford sediment: i.e., 6.08 for Na-boltwoodite or 12.2 for uranophane (Section 4.1). These new log K_{sp} values were used in subsequent kinetic modeling.

4.3. Modeling of Coupled Mass Transfer and Kinetic Dissolution

Uranyl mass transfer from intraparticle regions has been modeled previously using diffusion processes to describe the slow release of U(VI) from monazite ore (Olander and Eyal, 1990). The authors utilized a diffusion model with time-decreasing diffusivity to describe the dramatic decrease in the experimentally observed leaching rate with time. The solid phase in the diffusion model was assumed to be homogeneous. The fitted diffusivity was, however, many orders of magnitude higher than the diffusivity in the crystal lattice, suggesting that uranyl transport occurred through fractures in the rock matrix. It was suggested that the time-variable diffusivity indicated different degrees of fracture connectivity within the U-containing particles. A mass transfer limitation was also observed in uranyl leaching from soils (Braithwaite et al., 1997), where a decreasing release rate was modeled by a piecewise first-order kinetic expression with a first-order rate constant that decreased with time.

Our experimental observations of time variable U(VI) release rates combined with the microscopic observations of uranyl microprecipitates within intragrain fractures (Fig. 2) led us to construct a fracture-matrix diffusion model to describe U(VI) release from the intraparticle domain. The model included: i) diffusion within fractures that were well connected to the interparticle aqueous phase, and ii) diffusion in secondary, more removed fractures (henceforth referred to as *matrix*). The matrix diffusion model is conceptually representative of diffusion in an assemblage of smaller fractures and cleavages with poor intragrain connectivity, high tortuosity, or steric limitation. Uranyl microprecipitates in both fractures and the matrix were allowed to dissolve. The dissolved uranyl from the fractures was allowed to directly diffuse to the bulk solution, while that from the matrix was released to the fracture before diffusing to the bulk solution. The microscopic transport model was described as follows.

Fracture diffusion-dissolution for the aqueous phase

$$\frac{\partial C_f}{\partial t} = \left(\frac{D_f}{L_f^2}\right)\frac{\partial^2 C_f}{\partial l^2} + r_f - f_2 k_m (C_f - C_m) \tag{8}$$

Matrix diffusion-dissolution for the aqueous phase:

$$\frac{\partial C_m}{\partial t} = k_m (C_f - C_m) + r_m \tag{9}$$

Dissolution in the fractures of the solid phase:

$$\frac{\partial m_f}{\partial_t} = -r_f \tag{10}$$

Dissolution in the matrix of the solid phase:

$$\frac{\partial m_m}{\partial t} = -r_m \tag{11}$$

Mass balance in the sediment suspension:

$$\frac{dC_{sol}}{\partial t} = -f_1\frac{d\overline{C_f}}{dt} - f_1\frac{d\overline{m_f}}{dt} - f_1 f_2\frac{d\overline{C_m}}{dt} - f_1 f_2\frac{d\overline{m_m}}{dt} \tag{12}$$

where C_f and C_m are the aqueous concentrations in fracture and matrix, respectively; m_f and m_m are the precipitated concentrations normalized to the local pore volume in fracture and matrix, respectively; f_1 is the ratio of fracture pore volume vs. bulk aqueous solution volume; f_2 is the matrix and fracture pore volume ratio (matrix pore volume/fracture pore volume); and r_f and r_m are the kinetic rates of uranyl dissolution in the fracture and matrix, respectively, with the rate expression described by Eqn. 7; and l is the dimensionless length from fracture opening to the interior. A bar over concentration (e.g., $\bar{C}_f$) indicated a domain-averaged value. D_f/L_f^2 is the fracture diffusivity normalized to the half fracture length when both ends of the fracture are open to bulk solution, or the full fracture length when only one end is exposed. Parameter k_m is the mass transfer coefficient between the fracture and matrix.

Diffusion in the matrix was described using a first-order mass transfer model (Eqn. 9) to avoid the complication of matrix geometry. The length-normalized fracture diffusivity (D_f/L_f^2) was used as a single parameter in the model calculation because of the difficulty in separating diffusivity and fracture length. A similar approach was used to describe the influence of intraparticle diffusion on cesium desorption from Hanford sediments (Liu et al., 2003).

Eqns. 8 to 12 describe a microscopic U(VI) transport model from two intraparticle domains. The model does not account for the variable diffusivities of different U(VI) species. The diffusivity of charged aqueous species will be coupled with one another through the electrostatic diffusion potential. A more complete diffusion-reaction model could be assembled by coupling speciation reactions with the diffusivities of different charged species. However, this would involve more parameters at the microscopic level that would be difficult to determine independently. The diffusion model (Eqns. 8 to 12), coupled with U(VI) dissolution kinetics (Eqn. 7 using Na-boltwoodite to limit solubility with log K_{sp} = 6.08), was used to evaluate

Table 5. Dissolution/diffusion parameters for U(VI) release from Hanford sediments.

Sample	k (mol/L of $[HCO_3^-]_{tot})^{-1}h^{-1}$	k_m h^{-1}	D_f/L_f^2 h^{-1}	$1/f_2$
I53	0.066	0.0035	6.8	95
I61	0.066	0.0035	0.26	50
I67	0.066	0.0035	6.8	85

the relative importance of coupled diffusion and dissolution kinetics on uranyl release. The effects of diffusion of other species and uranyl sorption were incorporated into the apparent diffusivity and mass transfer coefficients (i.e., D_f and k_m) of U(VI).

The boundary condition at the particle surface was chosen to be the bulk solution concentration as a function of time. The measured concentration at the first sampling point (0.08 d) was used as the initial bulk solution concentration. A no flux condition was imposed at the interior ends of the fractures or at the middle of a two-end open fracture. The pore-water uranium concentration (Table 2) was used as the initial aqueous concentration within the fracture and matrix. The total uranium concentration (Table 1) was used as the initial solid uranium concentration after deducting the amount of uranium in the pore water. The solid phase uranium concentration was assumed to be homogeneous. Given this assumption, the parameter f_2 represented the initial mass ratio of U(VI) in the matrix and fracture $[U(VI)_m/U(VI)_f]$. The parameter f_1 was calculated to be 7.5×10^{-5} based on the experimental sediment-water ratio, an assumed 2.67 g/cm^3 solid density, and an intraparticle fracture volume of 0.1% estimated from SEM analysis of uranium-containing particles (McKinley et al., 2002). The initial bulk solution concentration was assumed to be zero for simulation of U(VI) dissolution in $(NH_4)_2CO_3$ electrolyte. The measured aqueous carbonate and silicate concentrations and pH (Appendix 1, Tables A1 to A5) were used in the dissolution simulation.

The coupled diffusion and dissolution model (Eqns. 7 to 9) was solved by a Crank-Nicholson finite difference scheme for concentrations in fracture and matrix (C_f and C_m), which were then used to update precipitated concentrations in fracture and matrix (m_f and m_m), and bulk concentration (C_{sol}) from Eqns. 10 to 12. The updated m_f, m_m, and C_{sol} were used to calculate C_f and C_m again from Eqns. 7 to 9. This process was iterated until convergence at every time step. A relative error of 1×10^{-6} was used to control global convergence of C_f, C_m, and C_{sol} for iteration. In the evaluation of kinetic dissolution rates (r_f and r_m) in Eqns. 8 to 11, the updated local C_f and C_m were used to calculate term IAP/K_{sp} in Eqn. 7. The Davies equation was used to calculate the activity coefficients for IAP evaluation. The model was used to simultaneously fit all experimental data in Figure 4 and Figure 5 by adjusting 4 parameters: the kinetic rate constant (k), the mass transfer coefficient (k_m), the normalized fracture diffusivity (D_f/L_f^2), and the uranyl mass ratio between fracture and matrix (f_2). After an optimal set of these parameters were estimated, we then finely tuned the parameters D_f/L_f^2 and f_2 to best match the experimental results for each sample while the parameters k and k_m were fixed at the same value for all samples. The fitted parameters are listed in Table 5.

The estimated fracture diffusivity value ($D_f/L_f^2 = 6.8$ h^{-1}) for sample I53 and I67 was on the order of molecular diffusivity of the uranyl ion in pure water (4.26×10^{-10} m^2/s) (Lide, 2003) when corrected by a tortuosity factor of 2.5 assuming the characteristic fracture length (L_f) of 0.3 mm. Sample I61 was different, however, and a much smaller diffusivity (Table 5) was needed to simultaneously fit the results in Figures 4 and 5. The estimated mass transfer coefficient (k_m) between the matrix and fracture was small. Using an approximate relationship of $k_m = D_m/L_m^2$ (Cussler, 1995) where D_m is the matrix diffusivity and L_m is the average diffusion distance in the matrix, respectively, the effective diffusivity in the matrix was estimated to be $D_m < k_m L_f^2 = 8.75 \times 10^{-14}$ m^2/s, which was over three orders of magnitude less than that in the fracture.

The dissolution rate constant (k) (Eqn. 7) of 0.066 $(mol/L)^{-1}h^{-1}$ (Table 5) was in the lower range of those reported in the literature for uranyl mineral dissolution (Table 6). Literature rate constants are typically normalized to surface area. We normalized the literature rate constants to total uranium concentration in Table 6 for comparative purposes because of the difficulty in measuring the surface area of intraparticle uranyl silicates in this study. Our dissolution rate constant [0.066 $(mol/L)^{-1}h^{-1}$] was about an order of magnitude lower than those of pure phase uranophane, soddyite, and $UO_3 \cdot H_2O$ (Table 6), but larger than that of U_3O_8.

Between 85 to 95% of the U(VI) in samples I53 and I67 was computed to exist in fractures with good connectivity to the

Table 6. Rate constants for uranyl mineral dissolution.

Mineral	Surface area m^2/g	Rate (mg U/m^2)/d	$[HCO_3^-]_{tot}$ mol/L	Rate constant[a] (mol/L of $[HCO_3^-]_{tot})^{-1}h^{-1}$	Source
Uranophane (flow-through)	35.4	0.06–2.0	0.001–0.02	0.09–0.72	1
Uranophane (batch)	35.4	0.82–16.3	0.001–0.02	0.25–5.14	1
Soddyite	25.4	2.5–25.3	0.008–0.02	0.47–2.52	2
U_3O_8	0.18	0.8–21	0.0002–0.02	0.004–0.06	3
$UO_3 \cdot H_2O$	0.32	100–700	0.0002–0.02	0.17–1.02	3
Na-Boltwoodite or uranophane			0.001–0.5	0.066	4

[a] The rate constant was normalized to total carbonate and total uranium concentrations at which the rate was determined (i.e., rate constant = rate $\times$ A $\times$ w/($[HCO_3^-]_{tot} \times 24000$), where A is the surface area of a uranium mineral, w = FW/($v \times 238.03$), FW is the formula weight and v is the stoichiometric coefficient of uranium in the formula for a uranyl mineral, respectively. 1. Perez et al. (2000); 2. Perez et al. (1997); 3. Steward and Mones (1997); 4. This study.

solution phase ($1/f_2$ in Table 5). This fraction decreased to 50% for I61. Dissolution in, and diffusion from these fractures controlled the dynamic picture of the kinetic profile from 0 to approximately 100 h (Fig. 6). The calculated time variable U(VI) concentrations in the fracture and matrix in Figure 6 were normalized to bulk solution volume [i.e., $(C_f + m_f)/f_1$, $(C_m + m_m)/(f_{1f2})$]. The fracture associated uranyl silicate was insufficient to saturate the aqueous phase with Na-boltwoodite or uranophane at pH $\approx$ 9 (Fig. 3). The remaining fraction of uranium was in the matrix and its transport to the aqueous phase occurred more slowly (Fig. 6). Using the model parameters in Table 5, we calculated that over 95 and 90% of total uranium in samples I53 and I67, respectively, was not subject to mass transfer limitation. The U(VI) release rate from these sediments was controlled by dissolution kinetics only. In contrast, only 40% of the precipitated U(VI) in sample I61 was computed to dissolve without mass transfer limitation, because of the lower apparent diffusivity of the fracture region. X-ray micrographs of samples I61 and I67 after 200 d of dissolution in electrolytes with pH 9.25 showed a contrast in the abundance of intragrain precipitates (Fig. 7).

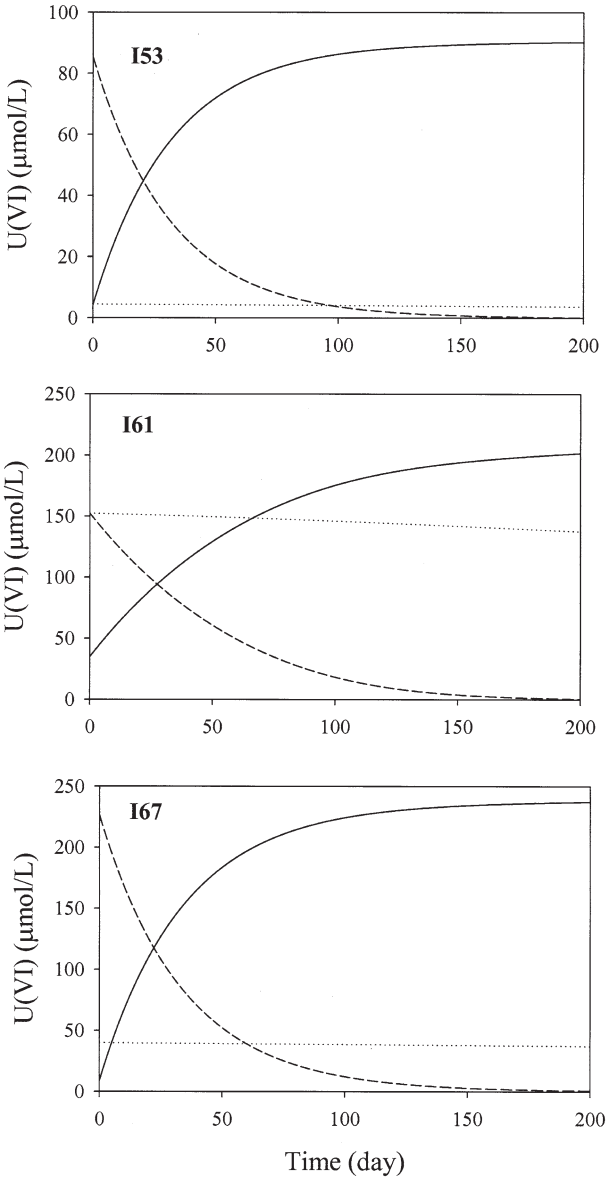

Fig. 6. Calculated U(VI) mass distribution in bulk solution (solid line), fractures (short dashed line), and the matrix domains (dotted line) corresponding to the dissolution experiment in Na-NO_3-HCO_3 electrolyte at pH 9.25 (Fig. 4). The time-variable U(VI) concentrations in the fracture and matrix domains were reported as normalized to bulk solution volume [i.e., $(C_{f+mf})/f_1$ for fracture, and $(C_m + m_m)/(f_{1f2})$ for matrix].

4.4. Implications for the Uranium Distribution Coefficient (k_d)

The distribution coefficient (K_d) is often used in performance assessment calculations to describe retardation extent through the retardation factor. Some adsorption processes exhibit a linear isotherm at low concentration, and for these, a single value of K_d can be used to describe the solid-liquid partitioning process as it controls retardation. Here, the K_d for uranium in the dissolution experiments was found to vary greatly with pH, bicarbonate/carbonate concentration, and contact time for all three sediments (Fig. 8). Values of K_d ranged from high values (e.g., $>$ 400 mL/g) where uranium would be virtually immobile, to lower values (e.g., 3.2 mL/g) where retarded mobility would occur. The K_d could also vary significantly with solid: solution ratio if this variable had been changed in the experiments, because the total amount of uranium that will dissolve from a solid phase is dependent on the volume of water in contact with it. These large variations in K_d result from the fact that uranium solid-liquid distribution is controlled by a kinetic release process that was collectively controlled by solubility saturation degree, dissolution kinetics, and mass transfer limitation. While our kinetic and solubility experiments were performed at 200 g/L, much higher ratios ($>2.7 \times 10^4$ g/L) exist in the Hanford vadose zone and larger in-situ K_d values would consequently result.

The large noted variation in K_d with pH change in BX-102 sediment (Fig. 8) indicates that a single value of K_d will not be an accurate predictor of uranium retardation in the BX-102 uranium plume. The measured pH values in the BX-102 core samples varied by over one unit at the end of the dissolution experiment (Appendix A, Tables A3 and A4) and measurements from proximate samples as received exhibited significantly different pH values (Serne et al., 2002). Moreover, the variations in K_d noted between the three sediments showed that K_d was a complex and dynamic function of precipitate distribution on and within sediment grains, and dissolution kinetics and mass transfer rates from intraparticle regions and grain coatings. These complex dependencies argue strongly against the use of K_d to forecast the future redistribution of the BX-102 plume unless a bounding calculation is desired. More sophisticated geochemical simulators that explicitly deal with the solubility, dissolution kinetics, and mass transfer rates are needed.

5. CONCLUSIONS

We were fortunate to obtain three low moisture content subsurface sediments from the Hanford site with micron-

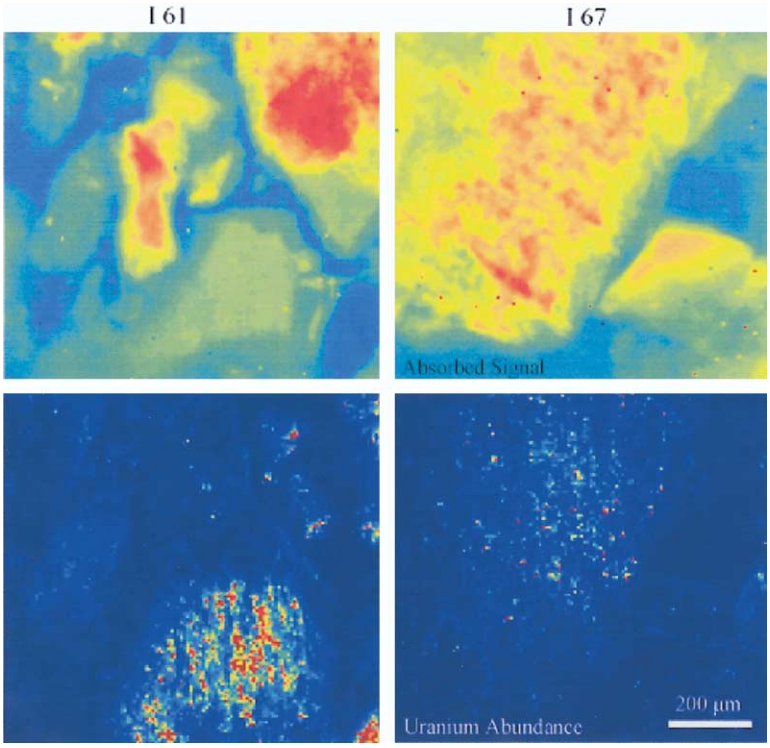

Fig. 7. False-color X-ray maps for the absorbance of X-ray beam flux (indicating the approximate sample grain geometry, top two panels) and for uranium abundance (red indicates the highest uranium abundance) in samples I61 and I67 (bottom two panels). The samples were measured after 200 d of uranyl dissolution.

sized intragranular precipitates of uranyl silicates. The mineralogic identity of the uranyl silicate has not been definitively determined but it exhibits spectral and solubility characteristics similar to Na-boltwoodite or uranophane. The sediment uranyl silicate dissolved slowly in electrolytes representative of the calcareous geochemical environments from which the sediments were obtained. Steady-state concentrations were not achieved at pH $>$ 8.2 even after 200 d of equilibration. A common pseudo–first-order rate constant could describe uranyl silicate dissolution kinetics in the three sediments over a range in pH, electrolyte composition, and bicarbonate/carbonate concentration. In spite of the intragrain residence of much of the precipitated U, dissolution kinetics, rather than intragrain mass transfer, appeared to regulate the slow release of U(VI) to the aqueous phase for two of the samples (I53, I67). Mass transfer was a major limitation on U(VI) release from one of the samples (I61). Physicochemical explanations for these differences were not readily apparent, but could result from minor lithologic variations or unknown geochemical or hydrologic aspects of the waste emplacement event which, itself, is not well understood (see McKinley et al., 2002).

A model linking dissolution kinetics and intragrain mass transfer was used to describe the time variant release of U(VI) from the sediments in different electrolytes. The model assumed a homogeneous intragrain distribution of U(VI) and the presence of two interconnected domains with different diffusivities that were termed fracture and matrix. The volume fractions of the two domains were obtained by data fitting. Although we conceptually described the matrix domain as one that was less accessible due to tortuosity and/or fracture fineness, this domain was not explicitly identified or characterized by microscopy. However, the important conclusion was that a physical construct containing two regions of differing diffusivity was required to model the data regardless of their physical conceptualization. The simplest explanation for our data is that the uranyl silicates were rapidly dissolved from grain surfaces and cavities, while the dissolution of intragrain precipitates was limited by distance from the grain surface and the associated longer diffusion time.

The studied sediments were taken from a vadose zone U(VI) plume that contains over 7000 kg of U(VI). The potential of this site to impact groundwater, and four or five more like it in different tank farms, is a major environmental concern at Hanford. The monitoring of groundwater some 30 m below the plume suggests the slow and incomplete release of sediment-bound U(VI) from the plume region. Groundwater concentrations are generally far below those that would result if adsorption (that typically yields K_d values in the range of 0.25 to 5 mL/g) was the primary retardation process in the plume. Our laboratory dissolution experiments, however, were consistent with the field observation and showed that the precipitated, intragrain U(VI) was released slowly to the aqueous phase. Reactive transport calculations coupling our measured dissolution rates for the uranyl silicates and intragrain diffusivities for the vadose zone lithic fragments, and appropriate geologic and hydrologic information for the vadose zone at this location are required to estimate uranium release rates from vadose zone to groundwater under various recharge scenarios.

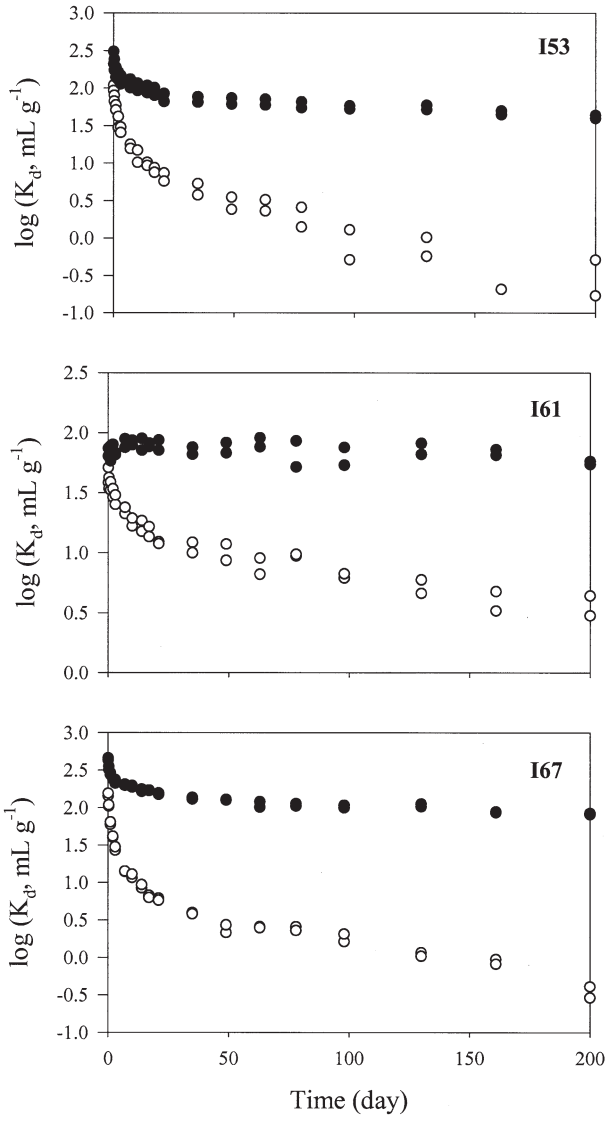

Fig. 8. Distribution coefficients (K_d) for uranium in kinetic dissolution experiments in Na-NO_3-HCO_3 electrolytes at pH of 7.27 (solid circle) and 9.25 (open circle) corresponding to experimental results in Figure 4 and Appendix 1, Table A3.

Acknowledgments—This research was supported by the U.S. Department of Energy (DOE) through the Environmental Management Sciences Program (EMSP) and the Hanford Remediation and Closure Science Project and the Hanford Vadose Zone Characterization Project managed by CH2M Hill providing the U(VI) contaminated sediments. Pacific Northwest National Laboratory (PNNL) is operated for the Department of Energy by Battelle. We thank Associate Editor Dr. Kathryn L. Nagy and three reviewers for their valuable comments and suggestions on the manuscript.

Associate editor: K. Nagy

REFERENCES

Aagaard P. and Helgeson H. C. (1982) Thermodynamic and kinetic constraints on reaction rates among minerals and aqueous solutions, 1. Theoretical considerations. *Am. J. Sci.* **282,** 237–285.

Allison J. D., Brown D. S., and Novo-Gradac K. J. (1998) MINTEQA2//PRODEFA2, a geochemical assessment model for environmental systems (version 4). Environmental Research Laboratory, U.S. EPA.

ASTM. (1988) *Standard Test Method for Total and Organic Carbon in Water by High Temperature Oxidation and by Coulometric Detection*. American Society for Testing and Materials.

Bargar J. R., Reimeyer R., and Davis J. A. (1999) Spectroscopic confirmation of uranium(VI)-carbonato adsorption complexes on hematite. *Environ. Sci. Technol*. **33,** 2481–2484.

Bargar J. R., Reimeyer R., Lenhart J. J., and Davis J. A. (2000) Characterization of U(VI)-carbonato ternary complexes on hematite: EXAFS and electrophoretic mobility measurements. *Geochim. Cosmochim. Acta* **64,** 2737–2749.

Braithwaite A., Livens F. R., Richardson S., and Howe M. T. (1997) Kinetically controlled release of uranium from soils. *Eur. J. Soil Sci*. **48,** 661–673.

Catalano J. G., Heald S. M., Zachara J. M., and Brown G. E. J. (2004) Spectroscopic and diffraction study of uranium speciation in contaminated vadose zone sediments from the Hanford site, Washington. *Environ. Sci. Tech.*, **38,** 2822-2828.

Chen F., Ewing R. C., and Clark S. B. (1999) The Gibbs free energies and enthalpies of formation of U^{6+} phases: An empirical method of prediction. *Am. Mineral*. **84,** 650–664.

Cussler E. L. (1995) *Diffusion: Mass Transfer in Fluid Systems*. Cambridge University Press.

Davis J. A., Payne T. E., and Waite T. D. (2002) Simulating the pH and pCO_2 dependence of uranium(VI) adsorption by a weathered schist with surface complexation models. In *Geochemistry of Soil Radionuclides,*pp. 61–86. Special Publication 59. SSSA.

De Pablo J., Casas I., Gimenez J., Molera M., Rovira M., Duro L., and Bruno J. (1999) The oxidative dissolution mechanism of uranium dioxide. I. The effect of temperature in hydrogen carbonate medium. *Geochim. Cosmochim. Acta* **63,** 3097–3103.

Duff M. C. and Amrhein C. (1996) Uranium(VI) adsorption on goethite and soil in carbonate solutions. *Soil Sci. Soc. Am. J*. **60,** 1393–1400.

Duff M. C., Mason C. F. V., and Hunter D. B. (1998) Comparison of acid and base leach for the removal of uranium from contaminated soil and catch box media. *Can. J. Soil Sci*. **78,** 675–683.

Duff M. C., Morris D. E., Hunter D. B., and Bertsch P. M. (2000) Spectroscopic characterization of uranium in evaporation basin sediments. *Geochim. Cosmochim. Acta* **64,** 1535–1550.

Duff M. C., Coughlin J. U., and Hunter D. B. (2002) Uranium coprecipitation with iron oxide minerals. *Geochim. Cosmochim. Acta* **66,** 3533–3547.

Fuhrmann M., Zhou H., Neiheisel J., Schoonen M. A. A., and Dyer R. (1997) Sorption/desorption of radioactive contaminants by sediment from the Kara Sea. *Sci. Total Environ*. **202,** 5–24.

Giammar D. E. and Hering J. G. (2001) Time scales for sorption–desorption and surface precipitation of uranyl on goethite. *Environ. Sci. Technol*. **35,** 3332–3337.

Grenthe I., Fuger J., Konings R. J. M., Lemire R. J., Muller A. B., Nguyen-Trung C., and Wanner H. (1992) *Chemical Thermodynamics.Vol. 1,Chemical Thermodynamics of Uranium*. OECD-NEA, Elsevier.

Guillaumount R., Fanghänet T., Neck V., Fuger J., Palmer D. A., Grenthe I., and Rand M. H. (2003)*Update on the Chemical Thermodynamics of Uranium, Neptunium, Pluytonium, Americium and Technetium*. Elsevier.

Heald S. M., Brewe D. L., Stern E. A., Kim K. H., Brown F. C., Jiang D. T., Crozier E. D., and Gordon R. A. (1999) XAFS and micro-XAFS at the PNC-CAT beamlines. *J. Synchrotron Radiat*. **6,** 347–349.

Hiskey J. B. (1979) Kinetics of uranium dioxide dissolution in ammonium carbonate. *Inst. Min. Metal. Trans.* **88,** c145.–c152.

Hiskey J. B. (1980) Hydrogen peroxide leaching of uranium in carbonate solutions. *Inst. Min. Metal. Trans.* **89,** c145.–c152.

Hsi C.-K. and Langmuir D. (1985) Adsorption of uranyl onto ferric oxyhydroxides: Application of the surface complexation site-biding model. *Geochim. Cosmochim. Acta* **49,** 1931–1941.

Hudson E. A., Terminello L. J., Viani B. E., Denecke M., Reich T., Allen P. G., Bucher J. J., Shuh D. K., and Edelstein N. M. (1999)

The structure of U^{6+} sorption complexes on vermiculite and hydrobiotite. *Clays Clay Miner*. **47,** 439–457.

Jones T. E., Simpson B. C., Wood M. I., and Corbin R. A. (2001) Preliminary inventory estimates for single-shell tank leaks in B, BX, and BY tank farms. CH2MHill Hanford Group, Richland, WA.

Kalmykov S. N. and Choppin G. R. (2000) Mixed $Ca^{2+}/UO_2^{2+}/CO_3^{2-}$ complex formation at different ionic strengths. *Radiochim. Acta* **88,** 603–606.

Langmuir D. (1978) Uranium solution-mineral equilibria at low temperatures with applications to sedimentary ore deposits. *Geochim. Cosmochim. Acta* **42,** 547–569.

Lenhart J. J. and Honeyman B. D. (1999) Uranium(VI) sorption to hematite in the presence of humic acid. *Geochim. Cosmochim. Acta* **63,** 2891–2901.

Lide D. R. (2003) *Handbook of Chemistry and Physics*. 84th ed CRC Press.

Liu C., Zachara J. M., Smith S. C., McKinley J. P., and Ainsworth C. C. (2003) Desorption kinetics of radiocesium from the subsurface sediments at Hanford site, USA. *Geochim. Cosmochim. Acta* **67,** 2893–2912.

Mason C. F., Turney W. R., Thomson B. M., Lu N., Longmire P. A., and Chisholm-Brause C. J. (1997) Carbonate leaching of uranium from contaminated soils. *Environ. Sci. Technol*. **31,** 2707–2711.

McKinley J. P., Zachara J. M., Smith S. C., and Turner G. (1995) The influence of uranyl hydrolysis and multiple site-binding reactions on adsorption of U(VI) to montmorillonite. *Clays Clay Miner*. **43,** 586–598.

McKinley J. P., Heald S. M., Zachara J. M., and Resch C. T. (2002) The identification of uranium-bearing phases by X-ray microprobe, electron microprobe, and scanning electron microscopy. In *Field Investigation Report for Waste Management Area B-BX-BY*. pp D122-D139. River Protection Project (RPP). RPP-10098, Prepared for the Office of River Protection by CH2M Hill Hanford Group, Richland, Washington.

Moll H., Geipel G., Matz W., Bernhard G., and Nitsche H. (1996) Solubility and speciation of $(UO_2)_2SiO_4$-H_2O. *Radiochim. Acta* **74,** 3–7.

Nguyen S. N., Silva R. J., Weed H. C., and Andrews J. E. J. (1992) Standard Gibbs free energies of formation at the temperature 303.15 K of four uranyl silicates: Soddyite, uranophane, sodium boltwoodite and sodium weeksite. *J. Chem. Thermodyn*. **24,** 359–376.

Nicol M. J. and Needes C. R. S. (1977) The anodic dissolution of uranium dioxide—II. in carbonate solution. *Electrochim. Acta* **22,** 1381–1384.

Ohnuki T., Isobe H., Yanase N., Nagano T., Sakamoto T., and Sekine K. (1997) Change in sorption-characteristics of uranium during crystallization of amorphous iron minerals. *J. Nucl. Sci. Technol*. **34,** 1153–1158.

Olander D. R. and Eyal Y. (1990) Leaching of uranium and thorium from monazite: II. Elemental leaching. *Geochim. Cosmochim. Acta* **54,** 1879–1887.

Payne T. E., Davis J. A., and Waite T. D. (1996) Uranium adsorption on ferrihydrite-effects of phosphate and humic acid. *Radiochim. Acta* **74,** 239–243.

Perez I., Casas I., Torrero M. E., Duro L., and Bruno J. (1997) Dissolution studies of soddyite as a long-term analogue of the oxidative alteration of the spent nuclear fuel matrix. *Mat. Res. Soc. Symp. Proc*. **465,** 565–572.

Perez I., Casas I., Martin M., and Bruno J. (2000) The thermodynamics and kinetics oaf uranophane dissolution in bicarbonate test solutions. *Geochim. Cosmochim. Acta* **64,** 603–608.

Riley R. G. and Zachara J. M. (1992) Chemical contaminants on DOE lands and election of contaminant mixtures for subsurface science research. U.S. Department of Energy, Office of Energy Research, Washington, DC.

Serne R. J., Bjornstad B. N., Gee G. W., Schaef H. T., Lanigan D. C., Lindenmeirer C. W., Orr R. D., LeGore V. L., Clayton R. E., Lindberg M. J., Kutnyakov I. V., Baum S. R., Geiszler K. N., Valenta M. M., Vickerman T. S., and Royack L. J. (2002) Characterization of Vadose zone sediment: Borehole 299-E33-46 near tank B-110 in the B-BX-BY waste management area. Pacific Northwest National Laboratory, Richland, WA.

Sharma J. N., Bhattacharya K., Swami R. G., Tangri S. K., and Mukherjee T. K. (1996) Studies of the kinetics of UO_2 dissolution in carbonate-bicarbonate medium using sodium hypochlorite as oxidant. *J. Radioanal. Nucl. Chem. Lett*. **214,** 223–233.

Shoesmith D. W., Sunder S., Bailey M. G., and Wallace G. J. (1989) The corrosion of nuclear fuel (UO_2) in oxygenated solution. *Corros. Sci*. **29,** 1115–1128.

Shoesmith D. W., Betteridge J. S., and Hocking W. H. (1996a) The cathodic reduction of oxygen on n-type UO2 in dilute alkaline aqueous solution. *J. Electroanal. Chem*. **406,** 69–81.

Shoesmith D. W., Sunder S., Bailey M. G., and Miller N. H. (1996b) The corrosion of used nuclear fuel in aqueous perchlorate and carbonate solutions. *J. Nucl. Mater*. **227,** 287–299.

Shoesmith D. W., Sunder S., and Tait J. C. (1998) Validation of an electrochemical model for the oxidative dissolution of used CANDU fuel. *J. Nucl. Mater*. **257,** 89–98.

Sowder A. G., Clark S. B., and Fjeld R. A. (1998) The effect of sample matrix quenching on the measurement of trace uranium concentrations in aqueous solutions using kinetic phosphorimetry. *J. Radioanal. Nucl. Ch*. **234,** 257–260.

Sowder A. G., Clark S. B., and Fjeld R. A. (2001) The impact of mineralogy in the U(VI)-Ca-PO_4 system on the environmental availability of uranium. *J. Radioanal. Nucl. Ch*. **248,** 517–524.

Steward S. A. and Mones E. T. (1997) Comparison and modeling of aqueous dissolution rates of various uranium oxides. *Mat. Res. Soc. Symp. Proc*. **465,** 557–564.

Sunder S., Shoesmith D. W., Kolar M., and Leneveu D. M. (1997) Calculation of used nuclear fuel dissolution rates under anticipated Canadian waste vault conditions. *J. Nucl. Mater*. **250,** 118–130.

Sylwester E. R., Hudson E. A., and Allen P. G. (2000) The structure of uranium(VI) sorption complexes on silica, alumina, and montmorillonite. *Geochim. Cosmochim. Acta* **64,** 2431–2438.

Turner G. D., Zachara J. M., McKinley J. P., and Smith S. C. (1996) Surface-charge properties and UO_2^{2+} adsorption of a subsurface smectite. *Geochim. Cosmochim. Acta* **60,** 3399–3414.

Waite T. D., Davis J. A., Fenton B. R., and Payne T. E. (2000) Approaches to modeling uranium(VI) adsorption on natural mineral assemblages. *Radiochim. Acta* **88,** 687–693.

Waite T. D., Davis J. A., Payne T. E., Waychunas G. A., and Xu N. (1994) Uranium(VI) adsorption to ferrihydrite: Application of a surface complexation model. *Geochim. Cosmochim. Acta* **58,** 5465–5478.

Wang Z., Zachara J. M., Gassman P. L., Liu C., Qafoku O., and Catalano J. G. (2004) Fluorescence spectroscopy of U(VI)-silicate and U(VI)-contaminated Hanford sediment. *Geochim. Cosmochim. Acta*, in press.

APPENDIX A

Selected Solutes Measured in Uranium Dissolution Experiments

Tables A1 and A2 show analyses of electrolyte solutions in the uranium solubility experiments (corresponding to the results in Fig. 3).[20]

Tables A3 and A4 shows analyses of electrolyte solutions in the kinetic dissolution experiments (corresponding to the results in Fig. 4 after 200 d of dissolution).

Table A5 shows analyses of 0.5 M $(NH_4)_2CO_3$ electrolyte after 19 d of extraction following 197 d of equilibration in Na-Ca-NO_3-HCO_3 electrolyte (pH 7.02) (corresponding to the results in Fig. 5).

Table A1. Selected solutes in Na-NO_3-HCO_3 electrolyte after 197 days of equilibration.

Sediment	pH[a]	pH[b]	UO_2^{2+} (μmol/L)	H_4SiO_4 (μmol/L)	PO_4^{3-} (μmol/L)	Na^+ (mmol/L)	Ca^{2+} (μmol/L)	Mg^{2+} (μmol/L)	$C_{inorganic}$ (mmol/L)	I[c]
BX-102	6.95	8.06	10.56	271.7	bd	49.87	864.6	336.6	1.620	0.05
I53	6.95	8.01	11.35	299.4	bd	49.33	880.5	374.9	1.631	0.05
	7.27	7.98	10.52	272.6	bd	44.50	825.3	318.4	1.616	0.05
	7.27	7.95	13.06	283.5	bd	46.45	829.8	343.2	1.598	0.05
	7.61	8.03	14.63	301.0	bd	51.20	752.0	360.4	1.737	0.05
	7.61	8.04	14.18	273.4	bd	51.85	730.8	307.7	1.858	0.05
	8.16	8.14	17.08	269.5	bd	47.61	513.5	220.8	2.166	0.05
	8.16	8.17	18.00	289.3	bd	50.28	522.5	297.5	2.153	0.05
	8.67	8.55	46.65	273.5	bd	47.63	213.6	161.9	5.234	0.05
	8.67	8.53	46.50	279.5	bd	49.28	262.5	212.9	4.661	0.05
	9.25	9.16	83.50	339.9	bd	46.89	56.10	115.9	20.16	0.05
	9.25	9.14	68.90	345.7	bd	43.93	49.60	118.2	19.63	0.05
BX-102	6.95	8.31	33.24	267.2	55.56	48.67	297.2	91.13	2.733	0.05
I61	6.95	8.29	32.06	253.7	60.26	47.54	324.0	87.62	2.612	0.05
	7.27	8.28	32.80	277.0	57.85	55.02	302.6	98.98	2.810	0.05
	7.27	8.34	34.06	320.6	67.14	55.24	283.6	98.11	2.854	0.05
	7.61	8.35	37.56	240.7	55.50	52.07	264.5	75.20	2.957	0.05
	7.61	8.37	36.93	218.8	56.95	51.94	255.1	71.33	3.100	0.05
	8.16	8.44	42.43	206.7	63.38	51.81	200.0	66.86	3.766	0.05
	8.16	8.43	44.47	236.6	59.08	51.72	193.6	73.76	3.836	0.05
	8.67	8.71	54.06	219.9	73.98	51.63	79.49	44.78	7.275	0.05
	8.67	8.73	59.49	241.7	83.14	50.89	81.80	50.67	7.671	0.05
	9.25	9.21	179.1	299.8	87.41	50.33	55.03	40.55	22.31	0.05
	9.25	9.21	189.4	288.4	96.89	50.59	59.34	36.18	22.42	0.05
BX-102	6.95	8.13	17.74	238.5	bd	47.64	798.5	177.2	1.663	0.05
I67	6.95	8.13	18.09	207.6	bd	49.89	811.6	168.7	1.699	0.05
	7.27	8.11	19.49	211.3	bd	49.80	784.2	173.7	1.716	0.05
	7.27	8.06	20.15	237.0	bd	49.46	791.0	186.6	1.689	0.05
	7.61	8.01	20.87	222.8	bd	49.85	699.2	172.8	1.798	0.05
	7.61	8.06	22.78	214.3	bd	49.72	711.1	157.8	1.826	0.05
	8.16	8.19	26.30	206.7	bd	50.15	493.5	125.8	2.299	0.05
	8.16	8.21	25.76	228.1	bd	51.33	514.2	148.5	2.319	0.05
	8.67	8.53	74.82	233.6	bd	46.98	218.3	83.47	5.036	0.05
	8.67	8.53	66.23	222.7	bd	48.15	195.2	61.97	5.084	0.05
	9.25	9.11	219.7	331.5	bd	47.24	64.51	49.67	20.00	0.05
	9.25	9.04	220.9	325.0	bd	46.85	71.95	51.64	19.86	0.05

[a] Electrolyte pH was the solution pH before contacting sediments (see Table 4).
[b] Suspension pH was the pH measured in the suspensions after 197 days of equilibration.
[c] Ionic strength in the suspensions after 197 days of equilibration. All solutes are total concentrations; bd: below detection limit.

Table A2. Selected solutes in Na-Ca-ClO_4-HCO_3 electrolyte after 197 days of equilibration.

Sediment	pH[a]	pH[b]	UO_2^{2+} (μmol/L)	H_4SiO_4 (μmol/L)	PO_4^{3-} (μmol/L)	Na^+ (mmol/L)	Ca^{2+} (μmol/L)	Mg^{2+} (μmol/L)	$C_{inorganic}$ (mmol/L)	I[c]
BX-102	7.59	7.44	12.46	283.4	bd	61.81	19.99	0.760	0.455	0.10
I53	7.59	7.24	11.76	256.5	bd	60.94	19.63	0.661	0.459	0.10
	8.05	7.92	12.12	258.1	bd	89.21	2.003	0.449	1.215	0.09
	8.05	7.93	11.14	244.8	bd	87.08	2.001	0.443	1.240	0.09
	8.35	8.20	24.81	246.8	bd	88.30	0.833	0.349	2.271	0.09
	8.35	8.19	25.48	252.1	bd	87.34	0.873	0.378	2.250	0.09
	8.37	8.11	20.57	294.5	bd	46.50	0.626	0.240	2.173	0.05
	8.37	8.11	18.67	253.9	bd	46.28	0.588	0.208	2.217	0.05
	8.96	8.69	55.79	261.0	bd	49.93	0.136	0.139	7.324	0.05
	8.96	8.61	55.82	295.3	bd	48.35	0.137	0.153	7.591	0.05
BX-102	7.59	7.68	43.53	302.1	bd	65.03	18.23	0.385	0.760	0.10
I61	7.59	7.72	40.14	293.9	bd	67.94	16.61	0.364	0.763	0.10
	8.05	8.12	34.74	243.9	44.94	88.34	1.025	0.155	1.729	0.09
	8.05	8.14	38.13	265.3	41.49	87.34	0.966	0.171	1.751	0.09
	8.35	8.42	47.21	227.9	54.77	90.87	0.299	0.112	3.396	0.09
	8.35	8.41	41.93	209.6	58.03	92.52	0.306	0.106	3.486	0.09
	8.37	8.21	46.11	246.6	64.22	49.67	0.190	0.071	3.726	0.05
	8.37	8.22	43.79	276.1	57.65	49.67	0.183	0.071	3.551	0.05
	8.96	8.71	67.65	259.2	72.64	52.07	0.060	0.044	10.59	0.05
	8.96	8.72	68.36	240.3	65.83	52.41	0.060	0.044	10.61	0.05
BX-102	7.59	7.44	19.63	237.0	bd	64.85	19.59	0.458	0.482	0.10
I67	7.59	7.46	19.35	251.4	bd	61.24	19.33	0.512	0.475	0.10
	8.05	7.90	18.11	226.6	bd	84.69	1.838	0.250	1.320	0.09
	8.05	7.88	21.29	241.9	bd	85.99	1.964	0.234	1.353	0.09
	8.35	8.18	42.44	215.9	bd	85.52	0.807	0.190	2.185	0.09
	8.35	8.14	43.19	265.1	bd	86.78	0.879	0.238	2.104	0.09
	8.37	8.11	37.43	231.3	bd	47.32	0.560	0.130	2.204	0.05
	8.37	8.15	37.20	223.8	bd	47.24	0.590	0.128	2.213	0.05
	8.96	8.65	141.8	265.9	bd	49.59	0.161	0.086	7.639	0.05
	8.96	8.52	124.2	231.5	bd	50.28	0.155	0.068	7.566	0.05

[a] Electrolyte pH was the solution pH before contacting sediments (see Table 4).
[b] Suspension pH was the pH measured in the suspensions after 197 days of equilibration.
[c] Ionic strength in the suspensions after 197 days of equilibration. All solutes are total concentrations; bd: below detection limit.

Table A3. Selected solutes in Na-NO_3-HCO_3 electrolyte after 200 days of equilibration.

Sediment	pH[a]	pH[b]	UO_2^{2+} (μmol/L)	H_4SiO_4 (μmol/L)	PO_4^{3-} (μmol/L)	Na^+ (mmol/L)	Ca^{2+} (μmol/L)	Mg^{2+} (μmol/L)	$C_{inorganic}$ (mmol/L)	I[c]
BX-102	7.27	8.13	10.52	261.8	bd	48.95	760.0	304.1	1.608	0.05
I53	7.27	8.07	9.524	253.2	bd	51.33	768.9	314.1	1.578	0.05
	9.25	9.07	83.62	295.2	7.026	46.32	54.80	104.2	20.96	0.05
	9.25	9.06	91.16	298.3	7.788	43.93	58.00	109.5	20.18	0.05
BX-102	7.27	8.31	26.98	255.2	51.91	47.24	200.0	69.60	2.348	0.05
I61	7.27	8.29	28.53	257.8	59.70	52.41	193.4	68.80	2.236	0.05
	9.25	9.19	210.7	333.1	102.9	49.76	58.70	42.40	22.79	0.05
	9.25	9.20	176.9	316.2	97.18	47.59	53.10	42.20	22.66	0.05
BX-102	7.27	8.08	15.32	236.4	bd	43.93	672.7	184.5	1.424	0.05
I67	7.27	8.08	15.70	233.5	bd	49.20	691.4	175.2	1.503	0.05
	9.25	9.09	250.7	315.1	bd	47.72	64.50	52.60	20.46	0.05
	9.25	9.08	248.2	323.8	bd	47.24	64.40	51.80	20.34	0.05

[a] Electrolyte pH was the solution pH before contacting sediments (see Table 4).
[b] Suspension pH was the pH measured in the suspensions after 200 days of equilibration.
[c] Ionic strength in the suspensions after 200 days of equilibration. All solutes are total concentrations; bd: below detection limit.

Table A4. Selected solutes in Na-Ca-ClO_4-HCO_3 electrolyte after 197 days of equilibration.

Sediment	pH[a]	pH[b]	UO_2^{2+} (μmol/L)	H_4SiO_4 (μmol/L)	PO_4^{3-} (μmol/L)	Na^+ (mmol/L)	Ca^{2+} (μmol/L)	Mg^{2+} (μmol/L)	$C_{inorganic}$ (mmol/L)	I[c]
BX-102	7.59	7.71	11.29	282.7	bd	56.67	18.28	0.790	0.503	0.10
I53	7.59	7.60	10.25	294.7	bd	53.81	18.72	0.789	0.453	0.10
	8.96	8.70	59.70	306.8	bd	45.76	0.153	0.170	7.406	0.05
	8.96	8.67	72.20	300.3	bd	48.80	0.173	0.164	7.613	0.05

[a] Electrolyte pH was the solution pH before contacting sediments (see Table 4).
[b] Suspension pH was the pH measured in the suspensions after 197 days of equilibration.
[c] Ionic strength in the suspensions after 197 days of equilibration. All solutes are total concentrations; bd: below detection limit.

Table A5. Selected solutes in $(NH_4)_2CO_3$ electrolyte after 19 days of extraction.

Sediment	pH[a]	pH[b]	UO_2^{2+} (μmol/L)	H_4SiO_4 (μmol/L)	PO_4^{3-} (μmol/L)	Na^+ (mmol/L)	Ca^{2+} (μmol/L)	Mg^{2+} (μmol/L)	$C_{inorganic}$ (mmol/L)
BX-102	8.43	8.95	84.27	156.8	15.01	0.311	88.09	49.31	0.425
I53	8.43	8.89	98.33	179.4	27.38	0.245	79.57	59.54	0.449
BX-102	8.43	8.92	215.8	187.6	102.5	0.371	83.19	44.93	0.432
I61	8.43	8.96	211.5	182.7	104.8	0.385	79.43	43.78	0.440
BX-102	8.43	8.85	230.8	215.8	20.05	0.290	85.31	44.33	0.458
I67	8.43	8.80	243.3	204.8	13.24	0.525	102.3	44.35	0.482

[a] Electrolyte pH was the solution pH before contacting sediments.
[b] Suspension pH was the pH measured in the suspensions after 19 days of equilibration. All solutes are total concentrations.

APPENDIX B

Calculated Uranyl Solubility in Uranium Dissolution Experiments

The calculated solubilities of Na-boltwoodite and uranophane were plotted in Figure 3, because they matched best with the experimental results.

Table B1. Calculated solubility (μmol/L U) of uranyl minerals in the sediment suspensions with Na-electrolyte.[a]

Sediment	Suspension pH	Na-boltwoodite	Soddyite	Uranophane	Na-Weeksite	Clarkeite	Becquerelite	Zellerite	Na-autunite
BX-102	8.06	5.735	94.12	11.93	94.12	94.12	48.56	94.12	56.95
I53	8.01	5.245	87.29	10.78	94.12	94.12	47.86	94.12	54.05
	7.98	5.747	82.67	10.99	94.12	94.12	44.58	94.12	51.42
	7.95	5.133	76.75	10.25	94.12	94.12	42.58	94.12	49.31
	8.03	5.543	94.12	12.68	94.12	94.12	53.48	94.12	58.40
	8.04	7.153	94.12	16.53	94.12	94.12	62.57	94.12	62.73
	8.14	10.90	94.12	26.47	94.12	94.12	88.72	94.12	85.03
	8.17	9.996	94.12	25.52	94.12	94.12	90.26	94.12	88.33
	8.55	94.12	94.12	94.12	94.12	94.12	94.12	94.12	94.12
	8.53	94.12	94.12	94.12	94.12	94.12	94.12	94.12	94.12
	9.16	94.12	94.12	94.12	94.12	94.12	94.12	94.12	94.12
	9.14	94.12	94.12	94.12	94.12	94.12	94.12	94.12	94.12
BX-102	8.31	21.85	339.5	61.40	233.2	267.1	165.6	339.5	121.9
I61	8.29	20.46	339.5	55.02	223.7	252.0	146.9	339.5	109.2
	8.28	20.53	339.5	63.70	225.4	270.7	175.5	339.5	116.4
	8.34	19.82	339.5	64.46	232.6	274.4	187.1	339.5	128.6
	8.35	29.45	339.5	83.82	263.9	293.7	203.4	339.5	144.8
	8.37	36.34	339.5	98.48	284.6	318.1	227.5	339.5	159.3
	8.44	63.72	339.5	159.1	339.5	339.5	339.5	339.5	234.2
	8.43	60.48	339.5	157.1	339.5	339.5	339.5	339.5	238.8
	8.71	284.8	339.5	339.5	339.5	339.5	339.5	339.5	339.5
	8.73	313.2	339.5	339.5	339.5	339.5	339.5	339.5	339.5
	9.21	339.5	339.5	339.5	339.5	339.5	339.5	339.5	339.5
	9.21	339.5	339.5	339.5	339.5	339.5	339.5	339.5	339.5
BX-102	8.13	9.023	260.7	21.28	150.1	160.8	62.09	274.8	75.74
I67	8.13	10.56	274.8	25.14	157.8	161.9	65.52	274.8	76.78
	8.11	10.49	274.8	25.35	156.7	167.8	66.06	274.8	75.87
	8.06	8.723	251.4	21.43	144.8	173.2	61.38	274.8	69.91
	8.01	10.28	274.8	26.33	150.3	201.6	68.61	274.8	69.14
	8.06	11.69	274.8	29.12	160.1	195.7	75.58	274.8	76.69
	8.19	23.65	274.8	60.80	214.0	256.4	137.0	274.8	120.0
	8.21	22.00	274.8	62.29	212.4	253.2	143.2	274.8	123.8
	8.53	183.7	274.8	274.8	274.8	274.8	274.8	274.8	274.8
	8.53	185.4	274.8	274.8	274.8	274.8	274.8	274.8	274.8
	9.11	274.8	274.8	274.8	274.8	274.8	274.8	274.8	274.8
	9.04	274.8	274.8	274.8	274.8	274.8	274.8	274.8	274.8
	9.06	274.8	274.8	274.8	274.8	274.8	274.8	274.8	274.8

[a] Calculated solubilities were limited by the total amount of U in the sediments. All of the U often dissolved at high pH.

Table B2. Calculated solubility (μmol/L U) of uranyl minerals in the sediment suspensions with Na-Ca-electrolyte.[a]

Sediment	Suspension pH	Na-boltwoodite	Soddyite	Uranophane	Na-Weeksite	Clarkeite	Becquerelite	Zellerite	Na-autunite
BX-102	7.44	5.378	61.52	3.315	94.12	94.12	20.10	94.12	30.49
I53	7.24	5.286	53.16	3.225	94.12	94.12	15.90	94.12	23.31
	7.92	3.056	94.12	7.678	82.58	87.08	34.92	94.12	39.66
	7.93	3.512	94.12	8.565	87.76	91.42	37.03	94.12	39.66
	8.20	11.57	94.12	38.22	94.12	94.12	94.12	94.12	94.12
	8.19	11.33	94.12	36.56	94.12	94.12	94.12	94.12	86.96
	8.11	11.03	94.12	24.16	94.12	94.12	89.95	94.12	86.96
	8.11	12.96	94.12	28.51	94.12	94.12	93.03	94.12	86.95
	8.69	94.12	94.12	94.12	94.12	94.12	94.12	94.12	94.12
	8.61	94.12	94.12	94.12	94.12	94.12	94.12	94.12	94.12
BX-102	7.68	20.81	145.3	14.85	117.5	165.7	69.28	339.5	83.02
I61	7.72	18.84	146.0	14.34	115.1	155.7	67.44	339.5	80.68
	8.12	6.066	270.8	19.58	131.2	109.5	65.11	339.5	49.79
	8.14	5.762	276.6	19.06	131.2	109.5	66.70	339.5	54.80
	8.42	37.31	339.5	134.9	302.7	310.7	309.8	339.5	185.1
	8.41	40.99	339.5	143.4	307.9	326.2	325.2	339.5	185.1
	8.21	45.54	339.5	126.1	294.2	339.5	302.4	339.5	156.0
	8.22	63.97	339.5	110.6	276.0	339.5	276.4	339.5	149.6
	8.71	339.5	339.5	339.5	339.5	339.5	339.5	339.5	339.5
	8.72	339.5	339.5	339.5	339.5	339.5	339.5	339.5	339.5
BX-102	7.44	4.508	61.37	3.235	74.19	133.6	16.04	274.8	31.03
I67	7.46	4.302	59.64	2.939	71.85	133.4	15.72	274.8	31.46
	7.90	3.600	173.8	10.33	96.86	99.77	35.68	274.8	41.78
	7.88	3.701	174.6	10.43	96.44	107.3	38.07	274.8	43.97
	8.18	15.54	274.8	52.59	188.7	183.5	126.8	274.8	108.7
	8.14	11.04	274.8	39.87	166.9	173.6	113.8	274.8	100.0
	8.11	19.74	274.8	48.67	198.9	261.8	116.8	274.8	109.9
	8.15	21.41	274.8	50.85	207.0	256.2	120.9	274.8	116.8
	8.65	274.8	274.8	274.8	274.8	274.8	274.8	274.8	274.8
	8.52	274.8	274.8	274.8	274.8	274.8	274.8	274.8	274.8

[a] Calculated solubilities were limited by the total amount of U in the sediments. All of the U often dissolved at high pH.